

# Chirp Parameter Selection for Affine Frequency Division Multiplexing with MMSE Equalization

Zunqi Li, *Graduate Student Member, IEEE*, Chuanbin Zhang, Ge Song, *Graduate Student Member, IEEE*, Xiaojie Fang, *Member, IEEE*, Xuejun Sha, *Member, IEEE* and Dirk Slock, *Fellow, IEEE*

**Abstract**—Affine Frequency Division Multiplexing (AFDM) is a chirp-transform modulation technique that has shown reliable performance in high-mobility scenarios, making it an attractive option for next generation communication systems. Recent literature suggests that under chirp parameter adjustment, AFDM can achieve optimal diversity performance in delay-doppler channels with maximum likelihood (ML) detection. However, the performance of AFDM with minimum mean square error equalization (MMSE-Eq) has not been extensively investigated in the existing literature. In this paper, we analyze the performance of AFDM with MMSE-Eq, derive a lower bound for the theoretical bit error rate (BER) of the AFDM system, and discuss the relationship between chirp parameters and performance degradation. To optimize BER performance, we propose two distinct chirp parameter selection strategies for frequency selective and doubly selective channels, respectively. These strategies offer the advantage of avoiding extensive computations. Additionally, we propose a low-complexity and high-performance iterative MMSE-Eq algorithm based on time-domain channel matrix operations. The algorithm resolves the issue encountered in existing low-complexity methods, where different chirp parameter selections significantly impact the complexity. Simulation results demonstrate the efficacy of our proposed parameter selection strategies and the outstanding BER performance achieved by the iterative MMSE-Eq algorithm.

**Index Terms**—Affine frequency division multiplexing, minimum mean square error (MMSE), channel equalization, doubly selective channel, frequency selective channel.

## I. INTRODUCTION

NEXT generation of wireless communication system, 6G, is expected to provide higher data rates and more reliable data transmission in many emerging high-speed mobility scenarios, such as Vehicle-to-Everything (V2X), railway communications, drone communications, Industrial Internet of Things (IIoT), as well as Space-Air-Ground-Underwater (SAGU) networks [2]. Typically, high-speed mobility scenarios are always accompanied by multi-path effects and

Part of the results appear in [1]. This work was supported in part by the National Natural Science Foundation of China (Grant 62171151 and U23A20278) and in part by the National Key Research and Development Program of China (Grant 2022YFB2902404). This research is also supported by Eurecom, France.

Zunqi Li, Chuanbin Zhang, Xiaojie Fang are with the School of Electronics and Information Engineering, Harbin Institute of Technology, Harbin, China and National Key Laboratory of Advanced Communication Networks, Shijiazhuang, China (e-mail: lizunqi@stu.hit.edu.cn; zhangchuanbin@stu.hit.edu.cn; fangxiaojie@hit.edu.cn). Ge Song, and Xuejun Sha are with the School of Electronics and Information Engineering, Harbin Institute of Technology, Harbin, China (e-mail: songge0621@163.com; shaxuejun@hit.edu.cn). Dirk Slock is with the Department of Communication Systems, EURECOM, 06410 Biot, France (e-mail: Dirk.Slock@eurecom.fr). The corresponding author is Xiaojie Fang.

Doppler spread, which significantly degrades the performance of traditional communication systems, such as Orthogonal Frequency Division Multiplexing (OFDM) and Cyclic Prefix-Single Carrier (CP-SC) systems [3]. Focusing on time domain or frequency domain modulation schemes is not sufficient in such challenging conditions. It is necessary to explore new modulation schemes that show strong robustness in high mobility scenarios.

### A. Related Works

Chirp-multicarrier modulation schemes have recently gained attention due to the energy spreading characteristics of chirp subcarriers in the time-frequency plane. This spreading allows for better resistance to interference and fading, making these modulation schemes particularly effective in challenging communication environments. One notable example is the fractional Fourier transform multicarrier (FRFT-MC) system, which was first proposed as a means of transferring information in the fractional time-frequency domain to counter the effects of doubly selective channels [4]. The implementation of FRFT-MC relies on the sampling-type discrete fractional Fourier transform (DFRFT) [5], which is derived from a sampled version of the continuous FRFT. The type of DFRFT exhibits low computational complexity similar to the fast Fourier transform (FFT). However, it lacks the property of unitarity, meaning that the subcarriers in FRFT-MC are unable to achieve perfect orthogonality, leading to inevitable information loss during transmission. Inspired by FRFT-MC, AFDM employs affine Fourier transform (AFT), a more general formulation of chirp transform, to construct a multicarrier modulation scheme [6]. More specifically, AFT can be made compatible with FRFT, Fresnel transform (FnT), and Fourier transform (FT) by adjusting the chirp parameters. Through the application of the discretization scheme given in [7], Discrete AFT (DAFT) can be fast implemented while preserving unitarity. Furthermore, [6] introduced the chirp-periodic cyclic prefix (CCP) and provided a strategy for selecting chirp parameters, significantly improving the reliability of the AFDM system. In their work [8], the authors derived both exact and approximate expressions for interference power in AFDM systems. Building upon this research, [9] investigated the impact of guard interval on system performance, which demonstrated that AFDM is capable of effectively reducing interference while maintaining high spectral efficiency.

Due to the fact that FnT can be regarded as a special case of AFT, the investigation of Orthogonal Chirp Division

Multiplexing (OCDM) systems can also offer insights and guidance for the advancement of AFDM systems. The digital implementation of OCDM relies on the discrete FnT, which produces an OCDM signal in the folded spectrum to maximize the spectral efficiency [10]. Since each chirp spans the entire signal band, unlike OFDM, it is hard to adjust the spectrum of OCDM signals by deactivating the edge chirp subcarriers. To flexibly design the spectrum of OCDM systems, a simple method is proposed in [11]. [12] investigated the performance of OCDM combined with different space-time codes and demonstrated through simulations that OCDM exhibited superior performance compared to OFDM in MIMO transmission.

### B. Comparison of AFDM, OTFS and OTSM

In addition to the chirp-multicarrier modulation schemes, Orthogonal Time Frequency Space (OTFS) and Orthogonal Time Sequence Modulation (OTSM) have also shown promising performance in high-mobility scenarios by mapping information in the delay-Doppler domain and delay-sequence domain, respectively. Similar to AFDM, these two modulation schemes are based on unitary transformations, ensuring orthogonal signal transmission. Another common feature among these modulations is their ability to separate channel path components based on the delay and Doppler spread, leading to optimal maximum likelihood (ML) detection performance [13], [14]. However, these schemes differ in four aspects: digital implementation complexity, Peak-to-Average Power Ratio (PAPR), pilot guard interval overhead, and parameter flexibility.

- Digital Implementation Complexity: OTSM has lower implementation complexity compared to OTFS and AFDM, as it avoids the use of FFT [15], [16].
- PAPR: OTFS and OTSM, being 2-D modulation schemes, avoid the superposition of all subcarriers, which reduces peak power and results in a lower PAPR compared to the chirp-multicarrier scheme AFDM [17].
- Pilot Guard Interval Overhead: The 2-D modulation schemes, OTFS and OTSM, require more pilot guard intervals to prevent interference between data and pilot, which gives AFDM an advantage in spectral efficiency due to its 1-D domain transmission [18].
- Parameter Flexibility: AFDM also benefits from the wide range of adjustable parameters due to its dual chirp parameter design, which OTFS and OTSM lack. This provides AFDM with advantages in secure transmission through parameter encryption [19] and superior sensing capabilities [20].

### C. Motivation and Contributions

To the best of our knowledge, the existing performance analysis of AFDM has primarily focused on ML detection and demonstrated the excellent performance of AFDM under this detection. However, the intractable complexity of ML detection makes it impractical for real-world applications and the corresponding diversity analysis cannot be extended to the linear equalizers. Therefore, we shift our focus to the more commonly used MMSE equalization (MMSE-Eq). As shown

in [21], [22], under MMSE-Eq in frequency-selective channels, each subchannel/subcarrier in CP-SC and OTFS can achieve equal Signal-to-Interference-and-Noise Ratio (SINR), leading to optimal transmission performance. Therefore, achieving equal SINR transmission has become a critical criterion for evaluating the performance of MMSE equalization. This motivated our research on parameter selection for AFDM, specifically exploring how to achieve equal SINR transmission across chirp subcarriers.

The contributions in this article are summarized below.

- We present the AFDM system models with MMSE-Eq in different domains, and demonstrate that their performance is equivalent. We take time-domain MMSE-Eq as an example and derive the theoretical lower bound of the BER for the AFDM system. Furthermore, we discuss how chirp parameters affect the performance degradation compared to the theoretical BER lower bound.
- We analyze the performance of the AFDM system with MMSE-Eq in both frequency selective channels and doubly selective channels, and provide corresponding parameter selection strategies. Based on optimal parameter selection, we demonstrate that AFDM can ensure equal SINR transmission for each subcarrier by adjusting the chirp parameters, closely approaching optimal BER performance under MMSE equalization.
- To enable AFDM systems to have flexibility in parameter selection, we proposed a low-complexity iterative equalization algorithm. It resolves complexity issues associated with fractional Doppler in multi-iteration scenarios, allowing each iteration to remain low in complexity without chirp parameter considerations. This algorithm significantly boosts performance compared to existing low complexity equalization algorithms for AFDM in doubly selective channels.

### D. Organization and Notation

The rest of the paper is organized as follows. Section II reviews basic AFDM concepts, which lay the foundations for the development of AFDM transmission and chirp selection strategies in Section III and IV. Low complexity iterative MMSE-Eq is presented in Section V. Simulations for the proposed parameter selection strategies and low complexity algorithm are presented in Section VI. Finally, conclusions are shown in Section VII.

We let  $b$  represent scalar,  $\mathbf{b}$  represent vector, and  $\mathbf{B}$  represent matrix.  $\mathbf{F}$ ,  $\mathbf{I}_N$ , and  $\mathbf{0}_N$  denote the  $N \times N$  discrete Fourier transform matrix, the identity matrix, and the zero matrix, respectively.  $(\cdot)^H$  represents the conjugate transpose, and  $(\cdot)^n$  denotes the  $n$ -th power.  $\text{diag}(\mathbf{b})$  returns a diagonal matrix where the diagonal elements are formed by the vector  $\mathbf{b}$ . On the other hand,  $\text{Diag}(\mathbf{B})$  returns a diagonal matrix where the diagonal elements are the same as the matrix  $\mathbf{B}$ .  $\text{tr}(\mathbf{B})$  returns the trace of  $\mathbf{B}$ . The notation  $[b]_N$  means taking the modulo operation of  $b$  with respect to  $N$ . The notation  $\lfloor b \rfloor$  means taking the floor operation applied to the value of  $b$ .  $\mathbf{B}_{(i,j)}$  represents the element in the  $(i+1)$ -th row and  $(j+1)$ -th column of matrix  $\mathbf{B}$ , and  $\mathbf{b}_{(i)}$  represent the  $(i+1)$ -th element of vectors  $\mathbf{b}$ .

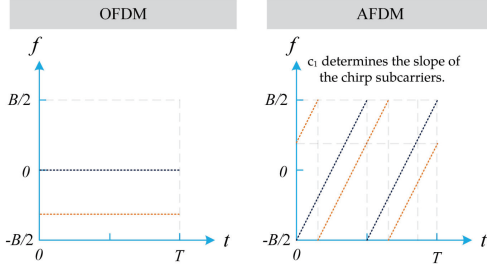


Fig. 1. The time-frequency representation of AFDM and OFDM subcarriers.

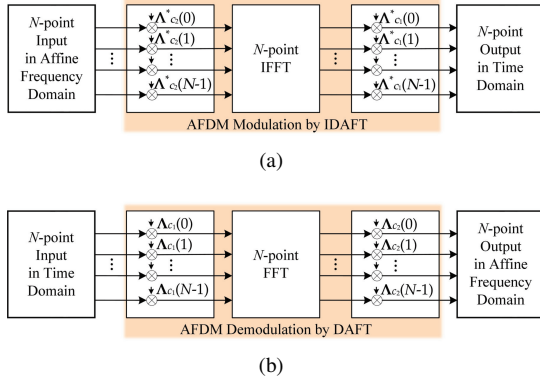


Fig. 2. The modulation and demodulation processes of AFDM. (a) Modulation. (b) Demodulation.

## II. PRELIMINARIES

### A. AFDM

AFDM is a chirp-based multicarrier communication system [6], [13], where each subcarrier is spread across the time-frequency plane. In contrast, traditional multicarrier systems like OFDM allocate each subcarrier to a specific frequency point. Due to this fundamental difference, AFDM demonstrates superior resilience to interference and fading compared to OFDM. The time-frequency representations of both systems are shown in Fig. 1.

Fig. 2 illustrates the modulation and demodulation processes of AFDM, as well as the signal mapping relationships. AFDM modulation maps the signal  $\{x_n, n = 0, 1, \dots, N-1\}$  from the affine frequency domain to the time domain using the Inverse Discrete Affine Fourier Transform (IDAFT), as shown below:

$$S_m = \frac{1}{\sqrt{N}} \sum_{n=0}^{N-1} x_n \varphi_n(m), \quad m = 0, 1, \dots, N-1, \quad (1)$$

where  $\varphi_n(m) = e^{j2\pi(c_1 n^2 + \frac{1}{N} mn + c_2 m^2)}$  represents the chirp orthogonal basis functions of IDAFT, and  $c_1$  and  $c_2$  represent the two chirp parameters that determine IDAFT and DAFT. The AFDM demodulation corresponds to the inverse transform of (1), which will not be detailed here.

The expression in (1) can be written in matrix form as  $\mathbf{s} = \mathbf{A}^H \mathbf{x}$ , where  $\mathbf{A}^H$  is the IDAFT matrix and  $\mathbf{A}$  is the DAFT matrix. The matrix  $\mathbf{A}$  can be computed using the diagonal matrices  $\mathbf{\Lambda}_{c_1}$  and  $\mathbf{\Lambda}_{c_2}$ , as well as the discrete Fourier matrix  $\mathbf{F}$ :

$$\mathbf{A} = \mathbf{\Lambda}_{c_2} \mathbf{F} \mathbf{\Lambda}_{c_1}, \quad (2)$$

where  $\mathbf{\Lambda}_c = \text{diag}(e^{-j2\pi c n^2}, n = 0, 1, \dots, N-1)$ , and  $\mathbf{F}$  can be efficiently computed using FFT. Compared to FFT, DAFT requires  $2N$  extra complex multiplication operations which results in a slight increase in complexity.

The digital implementation of AFT in (2) uses the same sampling rate configuration as OFDM, ensuring that AFDM occupies the same bandwidth as OFDM [10], as illustrated in Fig. 1. This characteristic ensures that the bandwidth remains unaffected by the system's chirp parameter settings.

### B. CCP

Inspired by OFDM's use of the cyclic prefix, AFDM similarly introduces the CCP to mitigate multipath effects. According to the chirp-periodicity [23], the CCP of AFDM systems can be represented as follows:

$$s_{n_{cp}} = s_{N+n_{cp}} e^{-j2\pi c_1 (N^2 + 2N n_{cp})}, \quad (3)$$

where,  $n_{cp} = -L_{cp}, -L_{cp} + 1, \dots, -1$  and  $L_{cp}$  is the length of the CCP, which should be no shorter than the maximum delay tap of the multipath channel, denote as  $l_p$ . When  $2Nc_1$  is an integer and  $N$  is even,  $e^{-j2\pi c_1 (N^2 + 2N n_{cp})} = 1$ , and  $s_{n_{cp}} = s_{N+n_{cp}}$ . In order to facilitate the subsequent analysis utilizing the properties of circulant matrices and to narrow down the parameter selection range, the chirp parameter  $c_1$  is assumed to be an integer divided by  $2N$  in the following discussion, making CCP equivalent to CP.

### C. Channel

The channel response can be described using a delay-Doppler channel representation,

$$h(\tau, \nu) = \sum_{i=1}^{N_{path}} h_i \delta(\tau - \tau_i) \delta(\nu - \nu_i), \quad (4)$$

where  $N_{path}$  is the number of paths,  $h_i$ ,  $\tau_i$ , and  $\nu_i$  are the complex path gain, delay, and Doppler shift associated with the  $i$ -th propagation path, respectively. Within the geometric coherent time, the physical propagation paths can be regarded as time-invariant [24], and it can be assumed that the delay and Doppler properties of the paths in (4) remain constant.

The delay tap  $l_i$  and Doppler-shift tap  $f_i$  for the  $i$ -th path can be obtained based on the system bandwidth  $B$  and subcarrier spacing  $\Delta f$  as follows:

$$l_i = B\tau_i, \quad f_i = \nu_i / \Delta f \quad (5)$$

Assuming that the Doppler shift tap of each path follows the Jakes spectrum, i.e.,  $\nu_i = f_c v \cos(\theta_i) / c$ , where  $f_c$  is the carrier frequency,  $v$  is the terminal speed,  $c$  is the speed of light, and  $\theta_i$  is uniformly distributed in the range  $[-\pi, \pi]$ . Given  $f_c = 6$  GHz,  $v = 550$  km/h, and  $\Delta f = 15$  kHz, the corresponding Doppler shift tap,  $|f_i| \leq 0.2$ , remains relatively small. To accommodate higher carrier frequencies, the specified subcarrier spacing in 5G NR is designed as a multiple of 15 kHz. Additionally, in wideband communications, the sampling interval resolution is sufficiently small, allowing fractional delay taps to be approximated as integer delay taps. Therefore, in the following discussion, doubly selective channels refer to

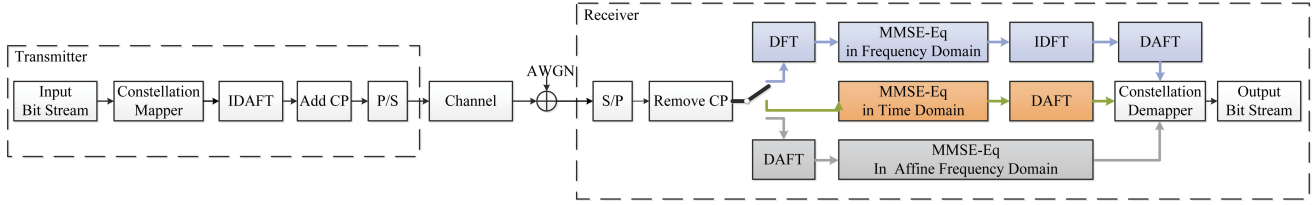


Fig. 3. Baseband system block diagram of the AFDM modulation with MMSE-Eq.

underspread channels with integer delay taps and fractional Doppler shift taps where  $|f_i| < 0.5$ .

According to [13], [25], the time domain channel matrix  $\mathbf{H}_t$  can be written as:

$$\mathbf{H}_t = \sum_{i=1}^{N_{path}} h_i \Delta_{f_i} \mathbf{\Pi}^{l_i}, \quad (6)$$

where  $\Delta_{f_i} = \text{diag}(e^{-j\frac{2\pi}{N}f_i n}, n = 0, 1, \dots, N-1)$ ,  $N_{path}$  represents the number of propagation paths, and  $\mathbf{\Pi}$  is the cyclic shift matrix

$$\mathbf{\Pi} = \begin{bmatrix} 0 & \cdots & 0 & 1 \\ 1 & 0 & \cdots & 0 \\ \vdots & \ddots & \ddots & \vdots \\ 0 & \cdots & 1 & 0 \end{bmatrix}_{N \times N}. \quad (7)$$

Additionally, simulations in [13] validate that, with the assistance of embedded pilot signals, the ML channel estimator for AFDM systems can accurately estimate  $h_i$ ,  $l_i$ , and  $f_i$ , enabling the precise reconstruction of  $\mathbf{H}_t$  in (6). Therefore, perfectly known  $\mathbf{H}_t$  is assumed in the subsequent derivations.

### III. AFDM TRANSMISSION WITH MMSE-EQ

#### A. System Model

We consider the baseband system of the AFDM modulation with MMSE-Eq depicted in Fig. 3, which is based on the assumption of perfect known channel state information and synchronization. The constellation mapper maps the bit stream to a symbol sequence  $\mathbf{x}$  from the  $M$ -ary constellation alphabet  $\mathcal{S} = \{\alpha_0, \alpha_1, \dots, \alpha_{M-1}\}$ . Then,  $\mathbf{x}$  is converted by the IDAFT operation into the time domain as  $\mathbf{s} = \mathbf{A}^H \mathbf{x}$ , where  $\mathbf{A}^H$  is the IDAFT matrix.

After removing the CCP at the receive end, the relationship between the transmitted signal  $\mathbf{s}$  and the received signal  $\mathbf{r}$  can be written as

$$\mathbf{r} = \mathbf{H}_t \mathbf{s} + \mathbf{n}, \quad (8)$$

where  $\mathbf{n}$  is complex-valued AWGN, with  $\mathbf{n} \sim \mathcal{CN}(\mathbf{0}, \sigma_n^2 \mathbf{I}_N)$ .

Then, MMSE-Eq in time domain is used to suppress the noise and interference of the received signal  $\mathbf{r}$ ,

$$\mathbf{u} = \mathbf{A} \mathbf{G}_t \mathbf{r} = \mathbf{A} \mathbf{G}_t \mathbf{H}_t \mathbf{A}^H \mathbf{x} + \mathbf{A} \mathbf{G}_t \mathbf{n}, \quad (9)$$

where  $\mathbf{u}$  denotes the estimated symbol sequence and  $\mathbf{G}_t$  denotes the equalization matrix in time domain,

$$\mathbf{G}_t = \mathbf{H}_t^H (\mathbf{H}_t \mathbf{H}_t^H + \sigma_n^2 \mathbf{I}_N)^{-1}. \quad (10)$$

MMSE-Eq matrices in frequency domain and affine frequency domain,  $\mathbf{G}_f$  and  $\mathbf{G}_{af}$ , can be obtained by replacing

$\mathbf{H}_t$  in (10) with the frequency domain channel  $\mathbf{H}_f = \mathbf{F} \mathbf{H}_t \mathbf{F}^H$  and the affine frequency domain channel  $\mathbf{H}_{af} = \mathbf{A} \mathbf{H}_t \mathbf{A}^H$ . The processes of above MMSE-Eq can be distinguished by the colors in Fig. 3. The estimated symbol sequence based on MMSE-Eq in frequency domain and affine frequency domain can be expressed as follows,

$$\begin{aligned} \mathbf{u}_f &= \mathbf{A} \mathbf{F}^H \mathbf{G}_f \mathbf{F} \mathbf{r}, \\ \mathbf{u}_{af} &= \mathbf{G}_{af} \mathbf{A} \mathbf{r}. \end{aligned} \quad (11)$$

According to (9) and (11), we have the following proposition.

*Proposition 1:* In AFDM systems, the performance of MMSE-Eq in different domains is the same, i.e.,  $\mathbf{u} = \mathbf{u}_f = \mathbf{u}_{af}$ .

*Proof:* Since both  $\mathbf{H}_f$  and  $\mathbf{H}_{af}$  can be represented by the time domain channel matrix  $\mathbf{H}_t$ , (11) can further be written as

$$\begin{aligned} \mathbf{u}_f &= \mathbf{A} \mathbf{F}^H \mathbf{F} \mathbf{H}_t^H \mathbf{F}^H (\mathbf{F} \mathbf{H}_t \mathbf{H}_t^H \mathbf{F}^H + \sigma_n^2 \mathbf{I}_N)^{-1} \mathbf{F} \mathbf{r} \\ &= \mathbf{A} \mathbf{H}_t^H (\mathbf{H}_t \mathbf{H}_t^H + \sigma_n^2 \mathbf{I}_N)^{-1} \mathbf{r} = \mathbf{u}, \\ \mathbf{u}_{af} &= \mathbf{A} \mathbf{H}_t^H \mathbf{A}^H (\mathbf{A} \mathbf{H}_t \mathbf{H}_t^H \mathbf{A}^H + \sigma_n^2 \mathbf{I}_N)^{-1} \mathbf{A} \mathbf{r} \\ &= \mathbf{A} \mathbf{H}_t^H (\mathbf{H}_t \mathbf{H}_t^H + \sigma_n^2 \mathbf{I}_N)^{-1} \mathbf{r} = \mathbf{u}. \end{aligned} \quad (12)$$

According to (12), it is easy to see that  $\mathbf{u} = \mathbf{u}_f = \mathbf{u}_{af}$ . ■

Based on *Proposition 1*, we choose MMSE-Eq in time domain to represent MMSE-Eq in other domains in the following content, for simplicity and clarity.

#### B. Derivation of the Lower Bound of BER

In the MMSE equalization receiver described above, the received signal for the  $i$ -th chirp subcarrier of the AFDM symbol is expressed as

$$\mathbf{u}_{(i)} = \underbrace{\mathbf{T}_{(i,i)} \mathbf{x}_{(i)}}_{\text{Signal}} + \underbrace{\sum_{j \neq i} \mathbf{T}_{(i,j)} \mathbf{x}_{(j)}}_{\text{Interference}} + \underbrace{\mathbf{n}'_{(i)}}_{\text{Noise}}, \quad i, j = 0, \dots, N-1 \quad (13)$$

where

$$\begin{aligned} \mathbf{T} &= \mathbf{A} \mathbf{G}_t \mathbf{H}_t \mathbf{A}^H, \\ \mathbf{n}' &= \mathbf{A} \mathbf{G}_t \mathbf{n}. \end{aligned} \quad (14)$$

From (13), the SINR of the  $i$ -th subcarrier can be expressed as

$$\beta_i = \frac{\mathbf{T}_{(i,i)}^2}{\text{Var}(\sum_{j \neq i} \mathbf{T}_{(i,j)} \mathbf{x}_{(j)} + \mathbf{n}'_{(i)})}, \quad (15)$$

where  $\text{Var}$  denotes the variance function.

When calculating SINR, it is common to utilize the Central Limit Theorem (CLT) and approximate the weighted sum of the interference as following a complex-valued normal distribution. Here, we adopt a simpler approximation method for calculating SINR (the detailed derivation can be found in the Appendix C of [22]),

$$\beta_i = \frac{\mathbf{T}_{(i,i)}}{1 - \mathbf{T}_{(i,i)}}. \quad (16)$$

In [22], the simplified relation in (16) is not used for further analysis. In this paper, we utilize this simplified relationship to investigate the performance of AFDM. Specifically, we focus on the diagonal elements of the equivalent matrix  $\mathbf{T}$ , which distinguishes our analysis from previous works.

The theoretical BER of PSK or QAM mapping with Gray coding can be approximated as a function of SINR, and the general expression of BER for the AFDM systems,  $P_{AFDM}$ , can be obtained by taking the average of the BER of each subcarrier,

$$\begin{aligned} P_{AFDM} &= \frac{1}{N} \sum_{i=0}^{N-1} a_M \text{erfc}(\sqrt{b_M \beta_i}) \\ &= \frac{1}{N} \sum_{i=0}^{N-1} a_M \text{erfc}\left(\sqrt{\frac{b_M \mathbf{T}_{(i,i)}}{1 - \mathbf{T}_{(i,i)}}}\right), \end{aligned} \quad (17)$$

where  $a_M$  and  $b_M$  depend on the mapping type [26], and  $\text{erfc}$ -function is defined as  $\text{erfc}(x) = \frac{2}{\sqrt{\pi}} \int_x^\infty e^{-t^2} dt$ .

If  $\phi(x) = \text{erfc}\left(\sqrt{\frac{b_M x}{1-x}}\right)$  is defined for  $0 < x < 1$ , then we have

$$\frac{d^2 \phi}{dx^2} = \frac{b_M e^{\frac{b_M x}{x-1}} (2b_M x - 5x + 4x^2 + 1)}{2x \sqrt{\pi} (x-1)^4 \sqrt{\frac{b_M x}{1-x}}}. \quad (18)$$

For QPSK mapping, where  $b_M = \frac{1}{2}$ , it can be easily proven that  $\frac{d^2 \phi}{dx^2} > 0$  for  $0 < x < 1$ , implying that the function  $\phi(x)$  is convex over the entire SINR range.

For other high-order PSK/QAM, the regions where convexity is maintained can be calculated based on  $b_M$ , which are

$$\begin{aligned} 0 < x &\leq \frac{5 - \sqrt{(2b_M - 1)(2b_M - 9)} - 2b_M}{8} \\ \text{and } \frac{5 + \sqrt{(2b_M - 1)(2b_M - 9)} - 2b_M}{8} &\leq x < 1. \end{aligned} \quad (19)$$

where the range  $0 < x \leq \frac{5 - \sqrt{(2b_M - 1)(2b_M - 9)} - 2b_M}{8}$  corresponds to the extremely low SINR region, while  $\frac{5 + \sqrt{(2b_M - 1)(2b_M - 9)} - 2b_M}{8} \leq x < 1$  corresponds to the high SINR region. The high SINR region typically falls within common SNR ranges, as demonstrated in [1], [10], ensuring that convexity can be guaranteed across a wide range of communication scenarios.

According to the convexity, we can use Jensen's inequality to obtain the lower bound of BER under MMSE-Eq,

$$\begin{aligned} P_{AFDM} &= \frac{1}{N} \sum_{i=0}^{N-1} a_M \text{erfc}\left(\sqrt{\frac{b_M \mathbf{T}_{(i,i)}}{1 - \mathbf{T}_{(i,i)}}}\right) \\ &\geq a_M \text{erfc}\left(\sqrt{\frac{b_M \sum_{i=0}^{N-1} \mathbf{T}_{(i,i)}/N}{1 - \sum_{i=0}^{N-1} \mathbf{T}_{(i,i)}/N}}\right) \triangleq P_{LB}. \end{aligned} \quad (20)$$

From Jensen's inequality, it is evident that the elements on the diagonal of matrix  $\mathbf{T}$  are equal when  $P_{AFDM} - P_{LB} = 0$ , i.e.,

$$\mathbf{T}_{(i,i)}^* = \sum_{i=0}^{N-1} \mathbf{T}_{(i,i)}/N = \frac{\text{tr}(\mathbf{T})}{N}, \quad (21)$$

where  $\mathbf{T}_{(i,i)}^*$  represents the ideal value of  $\mathbf{T}_{(i,i)}$  and  $P_{LB}$  can be represented as  $P_{LB} = a_M \text{erfc}\left(\sqrt{\frac{b_M \mathbf{T}_{(i,i)}^*}{1 - \mathbf{T}_{(i,i)}^*}}\right)$ . This is essentially equivalent to the viewpoint presented in [22], which states that the SINR in CP-SC is uniform across all subchannels in frequency selective channels. As a result, the theoretical BER of the CP-SC system can achieve  $P_{LB}$ .

## IV. CHIRP PARAMETER SELECTION

### A. Problem formulation

With the aim of minimizing the BER, we can formulate the problem of selecting chirp parameters as follows:

$$\begin{aligned} \min_{c_1, c_2 \in \mathbb{R}} \quad & P_{AFDM} - P_{LB} \\ \text{subject to} \quad & c_1 = \frac{k}{2N}, \end{aligned} \quad (22)$$

where  $k$  represents any integer.

*Proposition 2:* Given a deterministic channel, i.e., the channel response is perfectly known,  $P_{LB}$  for AFDM systems under MMSE-EQ does not change with the adjustment of chirp parameters.

*Proof:* Based on the cyclic property of the trace [27], we can obtain

$$\text{tr}(\mathbf{T}) = \text{tr}(\mathbf{A} \mathbf{G}_t \mathbf{H}_t \mathbf{A}^H) = \text{tr}(\mathbf{A}^H \mathbf{A} \mathbf{G}_t \mathbf{H}_t) = \text{tr}(\mathbf{G}_t \mathbf{H}_t). \quad (23)$$

It can be seen from (23) that the trace of the matrix is independent of  $\mathbf{A}^H$  and  $\mathbf{A}$ , so the adjustment of chirp parameters does not change the trace of  $\mathbf{T}$ , and  $P_{LB}$  remains unchanged. ■

According to *Proposition 2*, it can be considered that  $\mathbf{T}_{(i,i)}^*$  in equation (21) is independent of the chirp parameter, consequently,  $P_{LB}$  remains unchanged. Furthermore,  $P_{LB}$  is also independent of the unitary transform and only depends on the channel. This conclusion can be extended to other communication systems that rely on unitary transform matrix, such as rectangular pulse OTFS and OFDM systems.

$\mathbf{T}_{(i,i)}$  can be expressed as the result of making an alteration to the ideal value  $\mathbf{T}_{(i,i)}^*$ ,

$$\mathbf{T}_{(i,i)} = \mathbf{T}_{(i,i)}^* + \Delta\mathbf{T}_{(i,i)}, \quad (24)$$

where the size of the alteration is represented by  $\Delta\mathbf{T}_{(i,i)}$ , and  $\Delta\mathbf{T}_{(i,i)}$  can be seen as the cause of the degradation in transmission performance.

We rewrite (24) in matrix form

$$\text{Diag}(\mathbf{T}) = \text{Diag}(\mathbf{A}\mathbf{H}_{eq}\mathbf{A}^H) = \frac{\text{tr}(\mathbf{T})}{N}\mathbf{I}_N + \mathbf{\Lambda}_{\Delta\mathbf{T}}, \quad (25)$$

where

$$\mathbf{H}_{eq} = \mathbf{G}_t\mathbf{H}_t = \mathbf{H}_t^H(\mathbf{H}_t\mathbf{H}_t^H + \sigma_n^2\mathbf{I}_N)^{-1}\mathbf{H}_t \quad (26)$$

represents the equivalent channel matrix after MMSE-Eq, and  $\mathbf{\Lambda}_{\Delta\mathbf{T}}$  represents the diagonal matrix with  $\Delta\mathbf{T}_{(i,i)}$  on its diagonal.

$\mathbf{H}_{eq}$  can be decomposed as a sum of multiple matrices, as shown in the following formula:

$$\mathbf{H}_{eq} = \sum_{o=0}^{N-1} \mathcal{I}_o(\mathbf{H}_{eq}), \quad (27)$$

where  $\mathcal{I}_o(\mathbf{H}_{eq}) = \mathbf{\Pi}^o \circ \mathbf{H}_{eq}$ ,  $\circ$  denotes the Hadamard product, and  $\mathbf{\Pi}$  is the cyclic shift matrix shown in (7).

Substituting (27) into (14),  $\mathbf{T}$  can be divided into two parts,  $\mathbf{T}_D$  and  $\mathbf{T}_{OD}$ ,

$$\begin{aligned} \mathbf{T} &= \mathbf{A}\mathbf{H}_{eq}\mathbf{A}^H \\ &= \mathbf{A} \underbrace{\mathcal{I}_0(\mathbf{H}_{eq})}_{\text{Diagonal}} \mathbf{A}^H + \mathbf{A} \underbrace{\sum_{o=1}^{N-1} \mathcal{I}_o(\mathbf{H}_{eq})}_{\text{Off-Diagonal}} \mathbf{A}^H \\ &\triangleq \mathbf{T}_D + \mathbf{T}_{OD}. \end{aligned} \quad (28)$$

*Proposition 3:*  $\text{Diag}(\mathbf{T}_D)$  represents the diagonal matrix with the ideal value  $\mathbf{T}_{(i,i)}^*$  on its diagonal, i.e.,  $\text{Diag}(\mathbf{T}_D) = \frac{\text{tr}(\mathbf{T})}{N}\mathbf{I}_N$ .

*Proof:* Substituting (2) into (28), we can obtain

$$\mathbf{T}_D = \mathbf{\Lambda}_{c_2}\mathbf{F}\mathbf{\Lambda}_{c_1}\mathbf{H}_0\mathbf{\Lambda}_{c_1}^H\mathbf{F}^H\mathbf{\Lambda}_{c_2}^H = \mathbf{\Lambda}_{c_2}\mathbf{F}\mathbf{H}_0\mathbf{F}^H\mathbf{\Lambda}_{c_2}^H, \quad (29)$$

where  $\mathbf{H}_0 = \text{Diag}(\mathbf{H}_{eq})$ .

Based on the property of Fourier diagonalization, it can be deduced that the matrix  $\mathbf{F}\mathbf{H}_0\mathbf{F}^H$  is a circulant matrix. In a circulant matrix, the diagonal elements are completely identical, which means that  $\text{Diag}(\mathbf{F}\mathbf{H}_0\mathbf{F}^H) = \frac{\text{tr}(\mathbf{T})}{N}\mathbf{I}_N$ . Then, we can obtain  $\text{Diag}(\mathbf{T}_D) = \mathbf{\Lambda}_{c_2}\text{Diag}(\mathbf{F}\mathbf{H}_0\mathbf{F}^H)\mathbf{\Lambda}_{c_2}^H = \frac{\text{tr}(\mathbf{T})}{N}\mathbf{I}_N$ . ■

According to *Proposition 3* and (25), we can deduce that  $\text{Diag}(\mathbf{T}_{OD}) = \mathbf{\Lambda}_{\Delta\mathbf{T}}$ , which means that the performance degradation comes from  $\text{Diag}(\mathbf{T}_{OD})$ . In other words, when  $\text{Diag}(\mathbf{T}_{OD}) = \mathbf{0}_N$ , the BER achieves the lower bound, i.e.,  $P_{AFDM} = P_{LB}$ .

$\mathbf{T}_{OD}$  can be expressed as  $\mathbf{T}_{OD} = \sum_{o=1}^{N-1} \mathbf{T}_o = \sum_{o=1}^{N-1} \mathbf{A}\mathcal{I}_o(\mathbf{H}_{eq})\mathbf{A}^H$ , and the element in the  $(p+1)$ -th row and  $(q+1)$ -th column of  $\mathbf{T}_o$  is given by

$$\mathbf{T}_{o(p,q)} = \frac{1}{N}e^{j\frac{2\pi}{N}[Nc_1o^2 - qo + Nc_2(q^2 - p^2)]}\mathcal{F}_{o(p,q)}, \quad (30)$$

where

$$\mathcal{F}_{o(p,q)} = \sum_{n=0}^{N-1} h_{o,n}e^{-j\frac{2\pi}{N}(p-q+2Nc_1o)n}, p, q = 0, 1, \dots, N-1, \quad (31)$$

$h_{o,n}$  is the  $(n+1)$ -th element in the diagonal of  $\mathcal{D}_o(\mathbf{H}_{eq})$ , and  $\mathcal{D}_o(\mathbf{H}_{eq}) = \mathcal{I}_o(\mathbf{H}_{eq})(\mathbf{\Pi}^o)^{-1}$ .

Substituting  $p = q$  into (30), the element in the  $(p+1)$ -th row and  $(p+1)$ -th column of  $\mathbf{T}_o$  is given by

$$\mathbf{T}_{o(p,p)} = \frac{1}{N}e^{j\frac{2\pi}{N}(Nc_1o^2 - po)}\mathcal{F}_{o(p,p)}, \quad (32)$$

where  $\mathcal{F}_{o(p,p)} = \sum_{n=0}^{N-1} h_{o,n}e^{-j\frac{2\pi}{N}(2Nc_1o)n}$ . Specially, when  $c_1 = 0$ , the system is equivalent to OFDM, and  $\mathcal{F}_{o(p,p)} = \sum_{n=0}^{N-1} h_{o,n}$ ; when  $c_1 = \frac{1}{2N}$ , the system is equivalent to OCDM, and  $\mathcal{F}_{o(p,p)} = \sum_{n=0}^{N-1} h_{o,n}e^{j\frac{2\pi}{N}sn}$ .

It can be observed from (32) that the values of the diagonal elements  $\mathbf{T}_{o(p,p)}$  are independent of  $c_2$  and are related to the parameter  $c_1$ .

Now, the problem of minimizing  $P_{AFDM} - P_{LB}$  over  $c_1, c_2$ , subject to  $c_1 = \frac{k}{2N}$ , is equivalent to

$$\begin{aligned} \min_{c_1 \in \mathbb{R}} \quad & |\mathbf{T}_{OD(p,p)}| \\ \text{subject to} \quad & c_1 = \frac{k}{2N}, \end{aligned} \quad (33)$$

where  $\mathbf{T}_{OD(p,p)} = \sum_{o=1}^{N-1} \mathbf{T}_{o(p,p)}$  and  $k$  represents any integer.

### B. Chirp Parameter Selection in Frequency Selective Channels

In the previous section, the introduction of CCP in AFDM systems is given. For AFDM systems with CCP applied, the time-domain channel matrix  $\mathbf{H}_t$  is a circulant matrix under frequency selective channels, which realizes the convolution of the channel and the transmitted signal.

Due to the fact that the product of circulant matrices is still a circulant matrix, and the inverse of an invertible circulant matrix is a circulant matrix, it is easy to deduce that  $\mathbf{H}_{eq}$  is also a circulant matrix in frequency selective channels. This implies that  $h_{o,n} = h_{o,0}$  for  $n, o \in \Delta_N$ , where  $\Delta_N = \{1, 2, \dots, N-1\}$ , and we can obtain

$$\mathcal{F}_{o(p,q)} = \begin{cases} \sum_{n=0}^{N-1} h_{o,n} = Nh_{o,0}, & \text{if } [p-q+2Nc_1o]_N = 0 \\ \sum_{n=0}^{N-1} h_{o,0}e^{-j\frac{2\pi}{N}(p-q+2Nc_1o)n} = 0, & \text{else} \end{cases} \quad (34)$$

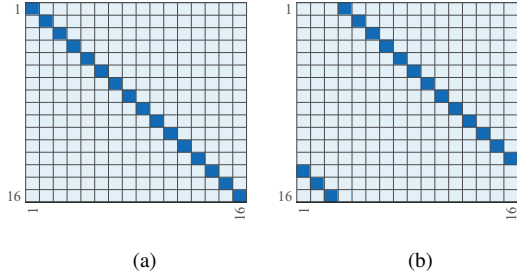


Fig. 4. The magnitudes of the elements in  $\mathbf{T}_{o=1}$  with different  $c_1$ . (a)  $c_1 = 0$ . (b)  $c_1 = \frac{3}{2N}$ .

It can be observed from (30) and (34) that each row in  $\mathbf{T}_o$  has only one non-zero element, and the relationship between the row and column of this non-zero element satisfies  $[p - q + 2Nc_1o]_N = 0$ .

Here, we take an example of a frequency selective 3-path channel, set  $N = 16$ , and chirp parameters  $c_1$  are selected as 0 and  $\frac{3}{2N}$ , respectively. Fig. 4 shows the magnitudes of the elements in  $\mathbf{T}_{o=1}$ . As can be seen from Fig. 4, the chirp parameter  $c_1$  can affect the elements of  $\mathbf{T}_o$ . More specifically, when  $c_1 = 0$ , the non-zero elements of  $\mathbf{T}_o$  are on the diagonal; when  $c_1 = \frac{3}{2N}$ , the positions of the non-zero elements move, and at this time all diagonal elements in  $\mathbf{T}_o$  are 0. This means that under the given  $o$ , a reasonable parameter  $c_1$  can ensure that the position of non-zero elements is not on the diagonal.

Substituting (34) into (32),  $\mathbf{T}_{OD(p,p)}$  can be expressed as

$$\begin{aligned} \mathbf{T}_{OD(p,p)} &= \sum_{o=1}^{N-1} \mathbf{T}_{o(p,p)} \\ &= \begin{cases} 0, & \text{if } [2Nc_1o]_N \neq 0, \forall o \in \Delta_N \\ \frac{1}{N} \sum_{o=1}^{N-1} e^{j\frac{2\pi}{N}(Nc_1o^2 - po)} \mathcal{F}_{o(p,p)}, & \text{else} \end{cases}. \end{aligned} \quad (35)$$

According to (33) and (35), when  $[2Nc_1o]_N \neq 0, \forall o \in \Delta_N$ , BER reaches the lower bound, which demonstrates that AFDM can achieve the same level of SINR transmission for each subcarrier as CP-SC in a frequency selective channel. We assume that the block length  $N$  is a power of 2, which is a common assumption in block length settings. For  $o \in \Delta_N$ , the product of odd numbers and  $o$  cannot be divisible by  $N$ , i.e.,  $[k_{\text{odd}}o]_N \neq 0$ , where  $k_{\text{odd}}$  represents any odd number. Therefore, in a frequency selective channel, choosing the optimal value of  $c_1$  as

$$c_1^* = \frac{k_{\text{odd}}}{2N}, \quad (36)$$

is a good option to minimize the BER. Importantly, the derivation of this parameter selection strategy relies on the circulant structure of the matrix rather than on deterministic channel impulse responses. As a result, given that the length of the transmission block,  $N$ , typically larger than maximum delay spread of the transmission path  $l_p$ , this parameter selection strategy does not require dependence on channel information and thus offers broad applicability.

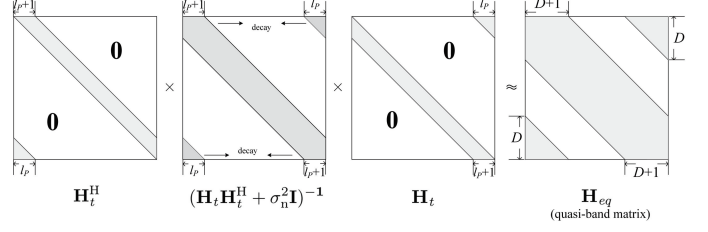


Fig. 5. The energy distribution of  $\mathbf{H}_{eq}$ .

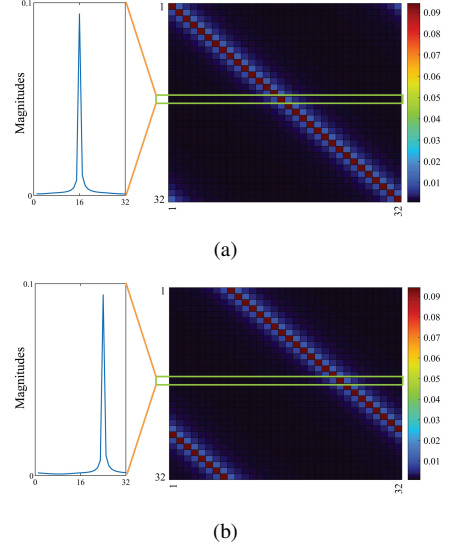


Fig. 6. The magnitudes of the elements in  $\mathbf{T}_{o=1}$  with different  $c_1$ . (a)  $c_1 = 0$ . (b)  $c_1 = \frac{8}{2N}$ .

### C. Chirp Parameter Selection in Doubly Selective Channels

The parameter selection strategy for doubly selective channels is similar to that for frequency selective channels, which involves analyzing the distribution of non-zero elements in the  $\mathbf{T}_o$  matrix and adjusting the parameter  $c_1$  to avoid non-zero elements appearing on the diagonal. However, due to the matrix inversion in  $\mathbf{G}_t$ , it is difficult to directly write out the exact expression for the sequence  $h_{o,n}, n = 0, 1, \dots, N-1$ , making it challenging to analyze how Doppler shift affects  $\mathbf{T}_o$ . To address this challenge, a chirp parameter selection strategy is proposed, which employs an approximate approach to efficiently analyze  $\mathbf{T}_o$ .

Since  $(\mathbf{H}_t \mathbf{H}_t^H + \sigma_n^2 \mathbf{I})$  is a sparse Hermitian matrix, according to [28], the inverse matrix elements will exhibit a rapidly decay in magnitude with increasing distance from the non-zero elements of the original matrix. From (26), the energy of  $\mathbf{H}_{eq}$  is mainly concentrated in three parts, as shown in Fig. 5: the banded matrix region, the lower triangular matrix region with size  $D \times D$ , and the upper triangular matrix region with size  $D \times D$ . The matrix elements in other regions can be approximated as zero, and the matrix  $\mathbf{H}_{eq}$  can be regarded as a quasi-band matrix with bandwidth of  $2D + 1$ . Then,  $\mathbf{T}_{OD}$

can be approximated as

$$\begin{aligned} \mathbf{T}_{\text{OD}} &\approx \mathbf{A} \left( \sum_{o=1}^D \mathbf{H}_o + \sum_{o=N-D}^{N-1} \mathbf{H}_o \right) \mathbf{A}^H \\ &= \sum_{o \in \Delta_D} \mathbf{T}_o, \end{aligned} \quad (37)$$

which allows us to focus solely on the distribution of non-zero elements in  $\mathbf{T}_o$  for  $o \in \Delta_D$ , where  $\Delta_D = \{1, \dots, D, N-D, \dots, N-1\}$ . In [29], similar approximation method has been used. Referring to their bandwidth setting, we set  $D = 2l_p$ .

*Observation 1:* The matrix elements in  $\mathbf{T}_o$  for  $o \in \Delta_D$  that have large magnitudes are mostly concentrated within a finite quasi-band region, where the relationship between their row and column indices satisfies  $\min([p-q+2Nc_1o]_N, N-[p-q+2Nc_1o]_N) \leq d_v$  with  $d_v$  serving as the threshold limit. For more detailed information about this observation, please refer to Appendix A.

We provide an example of a doubly selective channel, where we set  $N = 32$  and  $l_p = 3$ , and chirp parameters  $c_1 = 0$  and  $c_1 = \frac{8}{2N}$ . Fig. 6 shows the magnitudes of the elements in  $\mathbf{T}_{o=1}$ . Comparing Fig. 6 (a) with Fig. 4 (a), we can see that after introducing Doppler shift, the matrix  $\mathbf{T}_{o=1}$  no longer has only one non-zero element per row. The elements with large magnitudes are mainly concentrated within a quasi-band region, while the magnitudes in other regions are close to zero. From Fig. 6 (b), it can be observed that when  $c_1 = \frac{8}{2N}$ , the high-magnitude region has been shifted, thus avoiding these elements being located on the diagonal.

Based on the approximation assumption that high-magnitude elements are concentrated within a finite region, we obtain the following equation:

$$\begin{aligned} \mathbf{T}_{o(p,q)} &\approx 0, \\ \text{if } \min([p-q+2Nc_1o]_N, N-[p-q+2Nc_1o]_N) &> d_v. \end{aligned} \quad (38)$$

We define  $d_o = \min([2Nc_1o]_N, N-[2Nc_1o]_N)$  as a metric to describe the distance between high-magnitude region in  $\mathbf{T}_o$  and the diagonal. Based on the approximation in (37) and (38),  $\mathbf{T}_{\text{OD}(p,p)}$  can be expressed as

$$\begin{aligned} \mathbf{T}_{\text{OD}(p,p)} &= \sum_{o=1}^D \mathbf{T}_{o(p,p)} + \sum_{o=N-D}^{N-1} \mathbf{T}_{o(p,p)} \\ &\approx 0, \text{ if } d_o > d_v, \forall o \in \Delta_D. \end{aligned} \quad (39)$$

According to (33) and (39), if  $d_o > d_v, \forall o \in \Delta_D$ , we can obtain  $\text{Diag}(\mathbf{T}) \approx \frac{\text{tr}(\mathbf{T})}{N} \mathbf{I}_N$ , and BER approaches the lower bound. Due to the difficulty in obtaining an exact bound for the finite region, it is hard to directly determine the value of  $d_v$ . Therefore, we aim to keep the region of high-magnitude elements in  $\mathbf{T}_o$  for  $o \in \Delta_D$  as far away from the diagonal as possible. The parameter selection strategy can be expressed as follows:

$$c_1^* = \arg \max_{c_1} (d_{\min}). \quad (40)$$

where  $d_{\min} = \min([d_o, o \in \Delta_D])$  denotes the minimum distance between high-energy regions and the diagonal.

For a given value of  $D$ , an exhaustively search for  $c_1$  is not necessary. Instead, the following formula can be used to fast calculate  $c_1^*$ ,

$$c_1^* = \frac{\lfloor N/(D+1) \rfloor}{2N}. \quad (41)$$

In this case, the corresponding value of  $d_{\min}$  for  $c_1^*$  is  $\lfloor N/(D+1) \rfloor$ . Considering that the length of the transmission block,  $N$ , typically exceeds  $l_p$  significantly, and the Doppler shift satisfies  $|f_i| < 0.5$ , the parameter selection strategy in (41) can ensure optimal transmission in the underspread channels for AFDM systems.

## V. LOW-COMPLEXITY ITERATIVE EQUALIZER FOR AFDM

In this section, we propose a low-complexity and high-performance iterative LMMSE-Eq algorithm. This algorithm relies on the parameter selection strategy presented earlier, as the parameter selection strategy helps achieve excellent initial performance for iterative equalization. Additionally, the relationship  $\text{Diag}(\mathbf{T}) \approx \frac{\text{tr}(\mathbf{T})}{N} \mathbf{I}_N$ , obtained after optimizing the parameters, contributes to achieving low complexity, as will be discussed in the subsequent content.

### A. Iterative LMMSE Equalizer

Iterative LMMSE-Eq (I-MMSE-Eq) is widely used in communication systems [30], due to its remarkable ability to mitigate interference. As a soft-input soft-output equalizer, I-MMSE-Eq operates in two steps: 1) MMSE estimation based on the prior information, and 2) update of extrinsic information, which is then used to update the prior for the next iteration. With each iteration, the algorithm provides increasingly accurate information of the mean and covariance for MMSE estimation, effectively enabling soft interference cancellation.

In conventional I-MMSE-Eq, the inputs of each iteration are the mean  $\mathbf{m} = [\mathbb{E}(\mathbf{x}_{(0)}), \dots, \mathbb{E}(\mathbf{x}_{(N-1)})]^T$  and variance  $\boldsymbol{\eta} = [\mathbb{V}(\mathbf{x}_{(0)}), \dots, \mathbb{V}(\mathbf{x}_{(N-1)})]^T$  of the symbol sequence  $\mathbf{x}$ . A-prior information is needed to compute these input values, and the formulas are given as follows,

$$\begin{aligned} \mathbb{E}(\mathbf{x}_{(n)}) &= \sum_{\alpha_i \in \mathcal{S}} \alpha_i \cdot P(\mathbf{x}_{(n)} = \alpha_i), \\ \mathbb{V}(\mathbf{x}_{(n)}) &= \left( \sum_{\alpha_i \in \mathcal{S}} |\alpha_i|^2 \cdot P(\mathbf{x}_{(n)} = \alpha_i) \right) - |\mathbb{E}(\mathbf{x}_{(n)})|^2. \end{aligned} \quad (42)$$

The I-MMSE-Eq [30], [31] estimator  $\Phi_x$  for the  $l$ -th iteration can be expressed as:

$$\begin{aligned} (\boldsymbol{\mu}^{[l]}, \boldsymbol{\Sigma}^{[l]}) &= \Phi_x[\mathbf{y} = \mathbf{H}\mathbf{x} + \mathbf{n}], \\ \mathbf{x} &\sim \mathcal{CN}(\mathbf{m}^{[l]}, \text{diag}(\boldsymbol{\eta}^{[l]})), \mathbf{n} \sim \mathcal{CN}(\mathbf{0}, \sigma_n^2 \mathbf{I}_N), \end{aligned} \quad (43)$$

where

$$\begin{aligned} \boldsymbol{\mu}^{[l]} &= \mathbf{m}^{[l]} + \text{diag}(\boldsymbol{\eta}) \mathbf{H}^H \boldsymbol{\Psi}^{-1} (\mathbf{y} - \mathbf{H} \mathbf{m}^{[l]}), \\ \boldsymbol{\Sigma}^{[l]} &= \text{diag}(\boldsymbol{\eta}^{[l]}) - \text{diag}(\boldsymbol{\eta}^{[l]}) \mathbf{H}^H \boldsymbol{\Psi}^{-1} \mathbf{H} \text{diag}(\boldsymbol{\eta}^{[l]}), \end{aligned} \quad (44)$$

and  $\Psi = \mathbf{H} \text{diag}(\boldsymbol{\eta}^{[\ell]}) \mathbf{H}^H + \sigma_n^2 \mathbf{I}_N$ .

Given  $(\boldsymbol{\mu}^{[\ell]}, \boldsymbol{\Sigma}^{[\ell]})$ , the calculation of extrinsic information can be performed as follows,

$$\begin{aligned} \mathbf{m}_{E(n)}^{[\ell]} &= \frac{\boldsymbol{\mu}_{(n)}^{[\ell]} \boldsymbol{\eta}_{(n)}^{[\ell]} - \mathbf{m}_{(n)}^{[\ell]} \boldsymbol{\Sigma}_{(n,n)}^{[\ell]}}{\boldsymbol{\eta}_{(n)}^{[\ell]} - \boldsymbol{\Sigma}_{(n,n)}^{[\ell]}}, \\ \boldsymbol{\eta}_{E(n)}^{[\ell]} &= \frac{\boldsymbol{\Sigma}_{(n,n)}^{[\ell]} \boldsymbol{\eta}_{(n)}^{[\ell]}}{\boldsymbol{\eta}_{(n)}^{[\ell]} - \boldsymbol{\Sigma}_{(n,n)}^{[\ell]}}. \end{aligned} \quad (45)$$

Then, the external information in (45) is fed back into (42) as input for the next iteration. The updated probability is given by

$$P(\mathbf{x}_{(n)} = \alpha_i) \propto \exp \left[ \frac{-|\mathbf{m}_{E(n)}^{[\ell]} - \alpha_i|^2}{\boldsymbol{\eta}_{E(n)}^{[\ell]}} \right], \quad (46)$$

and satisfies the normalization condition  $\sum_{\alpha_i \in \mathcal{S}} P(\mathbf{x}_{(n)} = \alpha_i) = 1$ .

Repeatedly perform (42)-(46) until the set termination condition is met. In the final iteration, the algorithm utilizes  $\boldsymbol{\mu}$  from (44) to make the demapping decision.

It is noteworthy that the matrix  $\mathbf{H}$  varies across different communication systems. For instance, in CP-SC systems, the transform matrix is the identity matrix, and thus  $\mathbf{H} = \mathbf{H}_t$ . However, if iterative formulas are applied in an AFDM system, the scenario is different due to the introduction of AFT, and the matrix  $\mathbf{H}$  changes to  $\mathbf{H} = \mathbf{H}_t \mathbf{A}^H$ .

### B. Low-Complexity Solutions

Equation (44) constitutes the primary source of computational complexity in iterative equalization. For analytical convenience, we decompose it into three parts:  $\boldsymbol{\mu}^{[t=1]}$ ,  $\boldsymbol{\mu}^{[t>1]}$ , and  $\boldsymbol{\Sigma}^{[\ell]}$ . Next, we introduce a low-complexity algorithm, referred to as Time-domain Iterative MMSE-Eq (T-MMSE-Eq). This algorithm, based on the fast LU decomposition proposed in [32] and variance approximation, ensures that both  $\boldsymbol{\mu}^{[t=1]}$  and  $\boldsymbol{\mu}^{[t>1]}$  can be implemented with low complexity using the time-domain channel matrix. Furthermore, leveraging the earlier analysis regarding the approximate equality of  $\mathbf{T}_{i,i}$ , we facilitate fast computation of  $\boldsymbol{\Sigma}^{[\ell]}$ .

1) *Solution for  $\boldsymbol{\mu}^{[t=1]}$* : In the first iteration of I-MMSE-Eq or in the conventional MMSE-Eq, no a-priori information is available, therefore  $\mathbf{m}^{[1]} = \mathbf{0}_{N \times 1}$ ,  $\text{diag}(\boldsymbol{\eta}^{[1]}) = \mathbf{I}_N$ , and the matrix  $\mathbf{A}$  is eliminated during the calculation

$$\Psi = \mathbf{H}_t \mathbf{A}^H \mathbf{A} \mathbf{H}_t^H + \sigma_n^2 \mathbf{I}_N = \mathbf{H}_t \mathbf{H}_t^H + \sigma_n^2 \mathbf{I}_N. \quad (47)$$

In doubly selective channels, we can use fast LU factorization [32] to compute the inverse of the quasi-band matrix  $\Psi$ . This approach significantly reduces computational complexity without performance loss.

Fast LU factorization of  $\Psi$  is shown in Fig. 7 and the submatrices of  $\mathbf{L}$  and  $\mathbf{U}$  can be calculated using the following formula,

$$\begin{aligned} \Psi_1 &= \mathbf{L}_1 \mathbf{U}_1, \mathbf{U}_2 = \mathbf{L}_1^{-1} \Psi_3, \\ \mathbf{L}_2 &= \Psi_2 \mathbf{U}_1^{-1}, \mathbf{L}_3 \mathbf{U}_3 = \Psi_4 - \mathbf{L}_2 \mathbf{U}_2. \end{aligned} \quad (48)$$

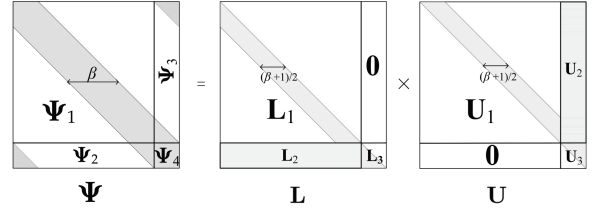


Fig. 7. Fast LU factorization of  $\Psi$ .

With the application of substitution algorithms in [32], and the fast algorithm of DAFT, we can complete the fast implementation of  $\boldsymbol{\mu}^{[1]}$  in the following calculation order,

$$\boldsymbol{\mu}^{[1]} = \mathbf{H}^H \Psi^{-1} \mathbf{y} = \underbrace{\mathbf{A} \mathbf{H}_t^H}_{(1)} \underbrace{\mathbf{U}^{-1} \mathbf{L}^{-1}}_{(2)} \mathbf{y}. \quad (49)$$

2) *Solution for  $\boldsymbol{\mu}^{[t>1]}$* : In subsequent iterations, each variance in  $\boldsymbol{\eta}$  is independently calculated and is no longer equal to each other. The matrix  $\mathbf{A}$  can no longer be eliminated during the calculation of  $\Psi$ , which is now expressed as  $\Psi = \mathbf{H}_t \mathbf{A}^H \text{diag}(\boldsymbol{\eta}^{[\ell]}) \mathbf{A} \mathbf{H}_t^H + \sigma_n^2 \mathbf{I}_N$ . This differs significantly from Equation (48). Consequently, we can rewrite  $\boldsymbol{\mu}^{[t>1]}$  as follows:

$$\boldsymbol{\mu}^{[t>1]} = \mathbf{m}^{[\ell]} + \mathbf{H}_{af}^H \Psi_{af}^{-1} \mathbf{A} (\mathbf{y} - \mathbf{H} \mathbf{m}^{[\ell]}) \quad (50)$$

where

$$\Psi_{af} = \mathbf{H}_{af} \text{diag}(\boldsymbol{\eta}^{[\ell]}) \mathbf{H}_{af}^H + \sigma_n^2 \mathbf{I}, \quad (51)$$

The complexity of factorizing  $\Psi_{af}$  depends on the bandwidth  $\beta$ , which is defined in Fig. 7. Moreover, the value of  $\beta$  in matrix  $\Psi_{af}$  is determined by  $\mathbf{H}_{af}$ . Considering the fractional Doppler shift,  $\mathbf{H}_{af}$  exhibits less sparsity compared to  $\mathbf{H}_t$  and changes with the variation of chirp parameters [13]. As a consequence, the value of  $\beta$  in matrix  $\Psi_{af}$  also changes with the variation of chirp parameters, leading to higher complexity in factorizing  $\Psi_{af}$ .

In order to avoid factorizing  $\Psi_{af}$  as done in [33], we substitute  $\bar{\eta}^{[\ell]} \mathbf{I}_N$  for  $\text{diag}(\boldsymbol{\eta}^{[\ell]})$ , and calculate (44) using the time-domain channel matrix,

$$\boldsymbol{\mu}^{[t>1]} = \mathbf{m}^{[\ell]} + \bar{\eta}^{[\ell]} \mathbf{A} \mathbf{H}_t^H \Psi_t^{-1} (\mathbf{y} - \mathbf{H} \mathbf{m}^{[\ell]}) \quad (52)$$

where

$$\Psi_t = \bar{\eta}^{[\ell]} \mathbf{H}_t \mathbf{H}_t^H + \sigma_n^2 \mathbf{I}_N, \quad (53)$$

and  $\bar{\eta}$  represents the mean value of sequence  $\boldsymbol{\eta}^{[\ell]}$ . The approximation of  $\text{diag}(\boldsymbol{\eta}^{[\ell]})$  with  $\bar{\eta}^{[\ell]} \mathbf{I}_N$  essentially treats the off-diagonal elements of the covariance matrix as zeros during the affine frequency domain to time domain transformation, which effectively prevents bandwidth  $\beta$  spreading. Due to the absence of off-diagonal elements, this approximation may result in slight performance degradation [34]. Nevertheless, considering the significant reduction in complexity, this approximation is acceptable.

3) *Solution for  $\Sigma^{[\ell]}$* : To compute the extrinsic information as shown in (45), only the diagonal elements of matrix  $\Sigma^{[\ell]}$  are required, which can be obtained by calculating

$$\text{Diag}(\Sigma^{[\ell]}) = (\bar{\eta}^{[\ell]}\mathbf{I}_N) - (\bar{\eta}^{[\ell]}\mathbf{I}_N)\text{Diag}(\mathbf{H}^H\mathbf{\Psi}_t^{-1}\mathbf{H})(\bar{\eta}^{[\ell]}\mathbf{I}_N). \quad (54)$$

It is worth noting that when computing (45), it is also necessary to replace  $\eta_{(n)}^{[\ell]}$  with  $\bar{\eta}^{[\ell]}$ .

Based on the performance analysis of AFDM presented in the previous section, it can be assumed that  $\text{Diag}(\mathbf{T}) \approx \frac{\text{tr}(\mathbf{T})}{N}\mathbf{I}_N \approx \mathbf{T}_{(1,1)}\mathbf{I}_N$  with a selected  $c_1^*$ , and this approximation can be further generalized to  $\text{Diag}(\mathbf{H}^H\mathbf{\Psi}_t^{-1}\mathbf{H}) \approx (\mathbf{H}^H\mathbf{\Psi}_t^{-1}\mathbf{H})_{(1,1)}\mathbf{I}_N$ . Therefore, we can compute only  $(\mathbf{H}^H\mathbf{\Psi}_t^{-1}\mathbf{H})_{(1,1)}$  instead of all diagonal elements. The calculation of  $(\mathbf{H}^H\mathbf{\Psi}_t^{-1}\mathbf{H})_{(1,1)}$  can follow a similar order as in (49), which is shown below,

$$\begin{aligned} (\mathbf{H}^H\mathbf{\Psi}_t^{-1}\mathbf{H})_{(1,1)} &= \mathbf{H}_{(1,:)}^H \mathbf{\Psi}_t^{-1} \mathbf{H}_{(:,1)} \\ &= (\mathbf{H}_t \mathbf{A}_{(:,1)}^H)^H \underbrace{\mathbf{U}^{-1} \mathbf{L}^{-1} (\mathbf{H}_t \mathbf{A}_{(:,1)}^H)}_{(1)}. \end{aligned} \quad (55)$$

### C. Complexity Analysis

Our low-complexity solutions effectively simplify the computational burden of (44). The primary complexities arise from four parts, which are (48), (49), (53), and (55). The comparison of complexity before and after using the low-complexity solutions in Section V-B is presented in TABLE I. From the table, it is evident that our low-complexity solutions significantly reduce the complexity, making them more suitable for transmissions with large block lengths  $N$ . The complexity of the proposed algorithm for  $l$  iterations is  $O(l[P_t^2 + \beta_t^2 + \log_2(N)]N)$ , where  $P_t$  denotes the number of non-zero elements in each row of the matrix  $\mathbf{H}_t$  and  $\beta_t = 2l_p + 1$  is the bandwidth of the Hermitian matrix  $\mathbf{\Psi}_t$ .

The existing low-complexity MMSE algorithm (LC-MMSE-Eq) for AFDM, as proposed in [33], performs low-complexity operations in the affine frequency domain. However, these operations exhibit significant complexity variations depending on changes in the chirp parameters, particularly when fractional Doppler shifts are considered. Let  $\beta_{af}$  denote the bandwidth of the Hermitian matrix  $\mathbf{\Psi}_{af}$ . The computational complexity of LC-MMSE-Eq is given by  $O(\beta_{af}^2 N)$ , where  $\beta_{af} = \min(4Nc_1l_p + 2k_v + 1, N)^1$ , and  $k_v$  is the minimum threshold for path separation under fractional Doppler shifts. With a large  $c_1$ , such as the parameter choice in (41),  $\mathbf{\Psi}_{af}$  lose their sparsity. As a result,  $\beta_{af}$  approaches  $N$  and the complexity of the existing algorithm increases to  $O(N^3)$ , which is significantly higher than that of the proposed algorithm under large block length transmissions.

In Fig. 8, we provide an illustration of matrix sparsity in the affine frequency domain and time domain. Specifically,  $\mathbf{\Psi}_t$  and  $\mathbf{\Psi}_{af}$  are compared under the same channel realization. For this comparison, we consider a doubly selective channel with

<sup>1</sup>To simplify the analysis, we assume that  $c_1 > 0$  and  $k_v$  is sufficiently large to ensure equalization performance.

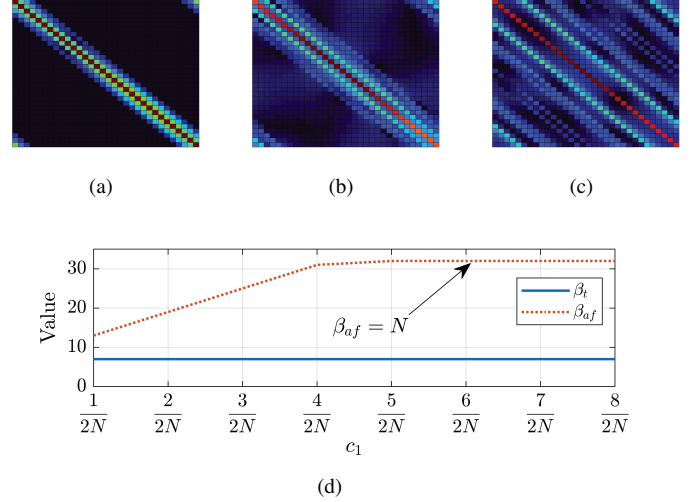


Fig. 8. An illustration of matrix sparsity in time domain and affine frequency domain. (a)  $\mathbf{\Psi}_t$ . (b)  $\mathbf{\Psi}_{af}$ ,  $c_1 = \frac{2}{2N}$ . (c)  $\mathbf{\Psi}_{af}$ ,  $c_1 = \frac{5}{2N}$ . (d) Comparison of  $\beta_t$  and  $\beta_{af}$  with different  $c_1$ .

TABLE I  
COMPARISON OF COMPLEXITIES.

Operation	Proposed T-MMSE-Eq		I-MMSE-Eq in (44)
$\mu^{[l]}$	(48)	$O(\beta_t^2 N)$	$O(N^3)$
	(49)	$O(\beta_t N + \log_2(N)N)$	
	(53)	$O(P_t^2 N)$	
$\Sigma^{[\ell]}$	(55)	$O(\beta_t N + P_t N)$	$O(\beta_t N^2 + P_t N^2)$

$N = 32$ ,  $l_p = 3$ , and  $k_v = 3$ . From Fig. 8 (a-c), we can observe that the matrix  $\mathbf{\Psi}_t$  exhibits greater sparsity and has a smaller bandwidth compared to  $\mathbf{\Psi}_{af}$  under different values of  $c_1$ . Furthermore, Fig. 8 (d) illustrates that the  $\beta$  value in  $\mathbf{\Psi}_t$  depends only on the time-domain channel matrix and is independent of AFT, while the  $\beta_{af}$  values in  $\mathbf{\Psi}_{af}$  increase as the chirp parameter  $c_1$  increases (until the band expansion fills the entire matrix, i.e.,  $\beta_{af} = N$ ). Consequently, compared to the low-complexity operations in the affine frequency domain, the time-domain low-complexity operations do not require considering the effects of fractional Doppler shifts and chirp parameters on  $\mathbf{\Psi}_{af}$ , leading to a more efficient approach.

## VI. SIMULATION RESULTS

In this section, we evaluate the BER performance of AFDM with MMSE-Eq under various chirp parameters to verify the effectiveness of the parameter selection. Additionally, we present simulation results of the proposed T-MMSE-Eq method. For the subsequent simulations, perfect channel state information is assumed at the receiver, and the channel model is based on (6). Specifically, it consists of uncorrelated Rayleigh fading paths, each with a uniformly distributed angle. The channel impulse responses follow two types of power delay profile (PDP): the exponential decay model [35] and the EVA channel model [36]. It is worth noting that in all the subsequent comparisons, we assume that the transmission

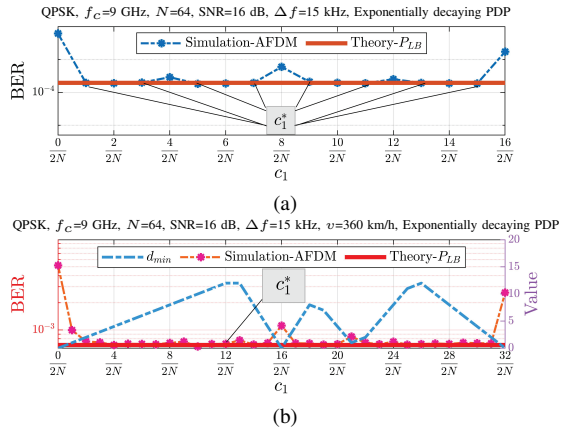


Fig. 9. An illustration of parameter selection strategy effectiveness. (a) In frequency selective channels. (b) In doubly selective channels.

blocks under different modulation schemes occupy the same bandwidth and time duration.

To validate the effectiveness of the parameter selection strategy, we present simulations for AFDM with MMSE-Eq in frequency selective channels ( $l_p = 7$ ) and doubly selective channels ( $l_p = 2$ ), respectively, as shown in Fig. 9. In frequency-selective channels, our parameter selection strategy avoids the potential performance degradation that may occur when  $2Nc_1o \neq k_{odd}$ , as demonstrated in Fig. 9 (a). For doubly selective channels, the parameter selection strategy does not focus on the parity but aims to maximize the distance  $d_{\min}$  by adjusting  $c_1$ . As shown in Fig. 9 (b),  $c_1^*$  corresponds to the maximum  $d_{\min}$ , effectively mitigating the significant performance degradation that may occur at lower  $d_{\min}$  values. For instance, small  $d_{\min}$  values at  $c_1 = 0, \frac{1}{2N}, \frac{16}{2N}, \frac{21}{2N}, \frac{32}{2N}$  can lead to noticeable increases in error rates. These results indicate that AFDM with the optimized parameters provided by (36) and (41) closely approaches optimal performance. It is noteworthy that our parameter selection strategies operate under the constraints of (35) and (39), offering a solution that avoids complex computations based on very limited channel prior information. This suggests that other parameter configurations may also enable the AFDM system to achieve excellent performance. With complete channel information, the value of  $D$  could be determined more precisely, rather than relying on the empirical value related to  $l_p$ , allowing for further optimization of the parameter selection strategy. However, subsequent simulations have validated that AFDM with our strategy approximates the lower bound exceptionally well, indicating that further performance improvements would be very limited.

In Fig. 10 (a), we demonstrate the performance of AFDM with MMSE-Eq under different chirp parameters in frequency selective channels. The performance of CP-SC, rectangular pulse OTFS [25], OTSM [14] with MMSE-Eq and  $P_{LB}$  in (20) are also shown for comparison. AFDM with  $c_1 = 0$  is equivalent to OFDM, in which case  $[2Nc_1o]_N = 0, \forall o \in \Delta_N$ . As a result, the system's performance is severely degraded, which can be observed from the worst performance shown in Fig. 10 (a). If  $c_1 = \frac{128}{2N}$ , then  $[2Nc_1o]_N = 0$  for all even values of  $o$ , which means that the performance degradation cannot be

completely avoided under this parameter setting. AFDM with  $c_1^* = \frac{3}{2N}$  can achieve equally good performance as CP-SC, OTFS, OTSM, and  $P_{LB}$ , which proves that this parameter selection strategy can ensure equal SINR for each subcarrier. At SNR=18 dB, OFDM achieves a BER that is comparable to the four mentioned modulation schemes operating at a lower SNR of 10 dB. The observed performance gap of 8 dB demonstrates the significant BER improvement provided by equal SINR transmission [22].

Fig. 10 (b) shows the performance of AFDM under doubly selective channels with different choices of chirp parameters. If  $c_1 = 0$  or  $c_1 = \frac{256}{2N}$ , it is evident that  $d_{\min} = 0$ . This means that the high energy region of  $\mathbf{T}_o$  does not move away from the diagonal, and thus AFDM performs poorly under these parameter choices. AFDM with  $c_1 = \frac{1}{2N}$  is equivalent to OCDM, where the minimum distance  $d_{\min} = 1$ . Although the performance degradation is less severe compared to the previous cases, there is still a noticeable 1 dB gain loss compared to the ideal performance at  $\text{BER} = 7 \times 10^{-5}$ . The BER performance of AFDM with  $c_1^*$  is close to  $P_{LB}$ , as shown in the figure. According to (41), we choose  $c_1^* = \frac{13}{2N}$  and verify that this parameter selection strategy effectively avoids performance degradation. The figure also illustrates the performance of CP-SC, OTFS and OTSM in doubly selective channels. The introduction of Doppler shift prevents CP-SC from achieving equal SINR transmission, resulting in a certain level of performance degradation. At  $\text{BER} = 1.5 \times 10^{-4}$ , CP-SC exhibits approximately a 2 dB performance gap compared to AFDM with optimized parameters. On the other hand, OTFS and OTSM demonstrate excellent performance with MMSE-Eq, exhibiting the same BER performance as AFDM. This affirms that OTFS and OTSM also possess the capability for equal SINR transmission. However, given that AFDM requires fewer pilot guard overheads and offers unique parameter flexibility, it emerges as a more competitive waveform in certain communication scenarios compared to 2-D modulation schemes.

Fig. 10 (c) and (d) illustrate the BER performance of the AFDM communication system under 16QAM mapping. It can be observed that the proposed parameter selection strategies remain effective, allowing AFDM to achieve performance comparable to OTFS, OTSM and  $P_{LB}$ . A noteworthy observation is that AFDM with  $c_1^*$  exhibits slightly worse performance compared to the OFDM in the low SNR region. This performance gap arises due to the convexity constraint imposed by high-order mapping in (19), which is more easily satisfied in the high SNR region. In contrast, QPSK mapping satisfies the convexity constraint across the entire SNR range. Therefore, the AFDM system with  $c_1^*$  consistently demonstrates the best performance under QPSK mapping.

Fig. 11 presents a comparison of the BER performance of the AFDM under different speed settings. The choice of  $c_1 = \frac{1}{2N}$  can be considered as a parameter selection strategy for frequency selective channels. It can be observed that in low-speed mobile scenarios where the Doppler shift effect is small, AFDM can achieve good performance even with parameter selection designed for frequency selective channels. As the moving speed increases, the performance gap between AFDM

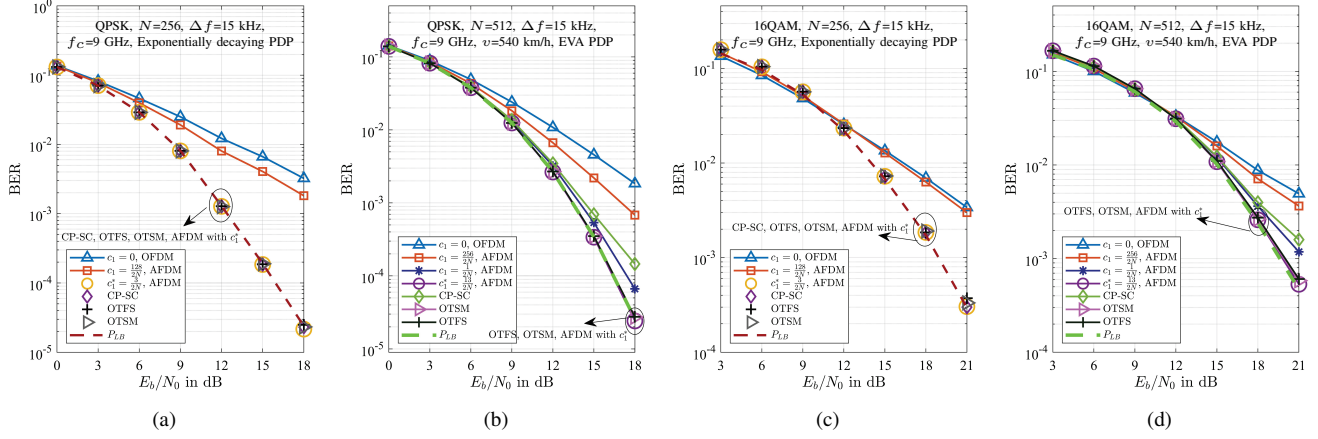


Fig. 10. BER performance of AFDM with different chirp parameters. (a) QPSK in frequency selective channels. (b) QPSK in doubly selective channels. (c) 16QAM in frequency selective channels. (d) 16QAM in doubly selective channels.

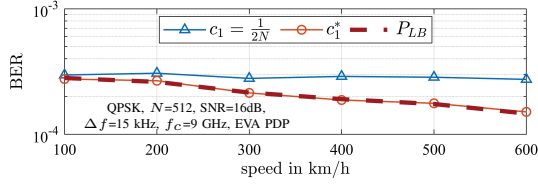


Fig. 11. BER performance of AFDM with different speed settings.

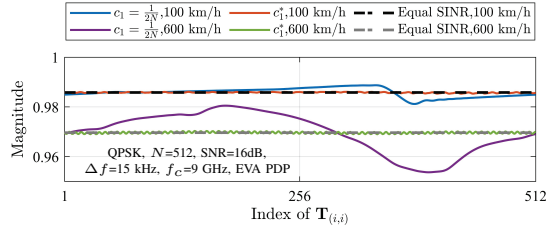


Fig. 12. The magnitudes of  $\mathbf{T}_{(i,i)}$  in doubly selective channels.

with  $c_1 = \frac{1}{2N}$  and  $c_1^*$  becomes more noticeable, as the impact of Doppler shift effect cannot be ignored. On the other hand, the choice of  $c_1^*$  based on (41) takes into account the Doppler effect and ensures that  $d_{\min}$  is as large as possible. Therefore, it achieves outstanding performance at different speeds.

As a supplement to Fig. 11, Fig. 12 depicts the magnitudes of  $\mathbf{T}_{(i,i)}$  under different parameters. According to (21), when  $\mathbf{T}_{(i,i)} = \frac{\text{tr}(\mathbf{T})}{N}$ , it can be considered that each subcarrier experiences equal SINR transmission. The optimized  $c_1^*$  ensures that  $\mathbf{T}_{(i,i)}$  is approximately equal under different speeds. Consequently, this implies an approximation of equal SINR transmission more closely in a simulated environment at a speed setting of 100 km/h. However, at a speed of 600 km/h, the magnitudes of  $\mathbf{T}_{(i,i)}$  under  $c_1 = \frac{1}{2N}$  exhibit more pronounced fluctuations.

In Fig. 13, we compare the BER performance of the LC-MMSE-Eq [33], conventional MMSE-Eq, I-MMSE-Eq and T-MMSE-Eq for AFDM systems. Additionally, OFDM, CP-SC, OTFS, and OTSM, as the most prominent waveforms

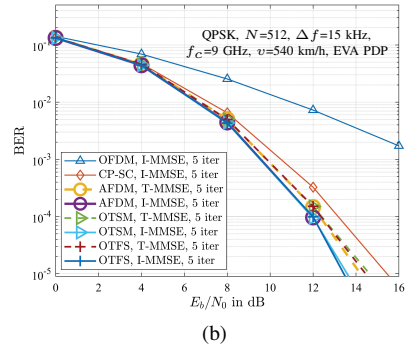
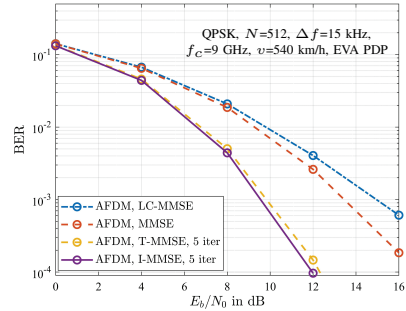


Fig. 13. The BER performance of (a) AFDM under different equalizers and (b) iterative equalizers under different modulation schemes.

today, are also included in the figure, with their respective BER performance depicted for comparison. It's worth noting that zero-padding is not applied in this simulation to ensure a fair comparison of BER while maintaining the same spectral efficiency. From Fig. 13 (a), it can be observed that AFDM with 5 iterations of I-MMSE-Eq outperforms the other algorithms, followed by our proposed T-MMSE-Eq, with approximately a 0.5 dB performance gap in the high SNR region. The performance difference between the two is due to the loss of information in the variance matrix when applying the low-complexity approximation. And LC-MMSE-Eq, fundamentally a modification of MMSE-Eq, approximates small elements induced by fractional Doppler shift in the affine

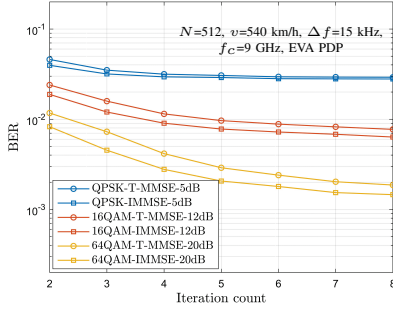


Fig. 14. Convergence behaviour of iterative equalizers for AFDM.

frequency channel matrix to zero. Therefore, LC-MMSE-Eq provides worse resilience to significant fractional Doppler shifts than conventional MMSE-Eq. In summary, the proposed algorithm significantly reduces the complexity of I-MMSE-Eq with only a slight performance loss. Compared to the existing LC-MMSE, it offers both lower complexity and superior performance.

According to the simulation results in Fig. 10 (b), it can be seen that both OTSM and OTFS have the potential to achieve equal-SINR transmission. Since the proposed low-complexity algorithm is based on the equal-SINR transmission property, it can also be applied to OTSM and OTFS. In Fig. 13 (b), AFDM, OTSM and OTFS achieve very similar performance under both T-MMSE-Eq and I-MMSE-Eq. However, OFDM and CP-SC fail to provide strong initial performance, which limits the improvement of their iterative performance. Compared to the other three waveforms, OFDM shows a performance gap of over 10 dB at  $\text{BER} = 2 \times 10^{-3}$ , while CP-SC has a gap of around 1 dB at  $\text{BER} = 3 \times 10^{-4}$ .

Fig. 14 illustrates the convergence of the iterative MMSE-Eq algorithms. It can be observed that, under different constellation mappings, the algorithm exhibits good convergence. Specifically, there is a significant improvement in BER with a small number of iterations. As the number of iterations increases ( $l \geq 5$ ), the performance improvement becomes marginal. To further improve BER performance or reduce the number of iterations required for convergence, additional measures such as channel coding are required. The extent of enhancement depends on the chosen channel coding scheme, which can be adjusted to balance performance gains with computational efficiency. In the low SNR region, due to the inability to exchange reliable external information, the performance of T-MMSE-Eq and I-MMSE-Eq is quite close. However, at high SNR region, a notable performance difference emerges between the two algorithms. I-MMSE-Eq achieves excellent performance with fewer iterations. However, considering the significantly reduced complexity, the proposed algorithm is more suitable for practical applications.

## VII. CONCLUSION

In this paper, we investigate the impact of different parameters on the performance of the AFDM system. We propose two parameter selection strategies specifically designed for

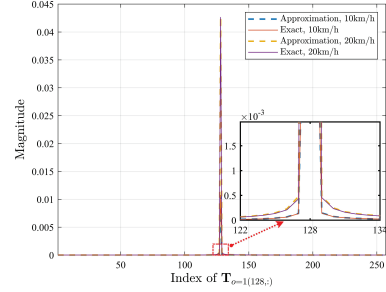


Fig. 15. The magnitudes of the elements in  $\mathbf{T}_{o=1(128,:)}$  with  $c_1 = 0$  obtained by approximated method and exact method.

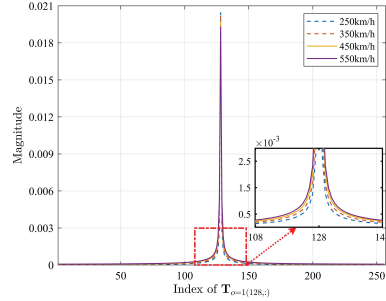


Fig. 16. The magnitudes of the elements in  $\mathbf{T}_{o=1(128,:)}$  with  $c_1 = 0$  for high speed settings.

frequency selective and doubly selective channels, respectively. For frequency selective channels, the parameters can be selected independently of the channel. While dealing with doubly selective channels, the strategy necessitates knowledge of the maximum path delay in the channel. These parameter selection strategies eliminate the need for complex matrix operations and exhaustive search, making them more practical for applications. Additionally, we introduce a T-MMSE-Eq algorithm that utilizes the time-domain channel matrix, thus eliminating the need to account for variations in chirp parameters. This algorithm achieves high performance through multiple iterations of MMSE estimation, while still maintaining low computational complexity. In conclusion, all of the aforementioned approaches effectively enhance the implementation of AFDM with MMSE-Eq and demonstrate outstanding performance. In future work, it is worth considering the research of jointly applying MMSE-Eq and channel coding in AFDM systems for Turbo equalization.

## APPENDIX A EXTENSIONS OF OBSERVATION 1

We rewrite the time-varying channel in (6) as

$$\begin{aligned} \mathbf{H}_t &= \sum_{i=1}^P h_i \mathbf{\Pi}^{l_i} [\mathbf{I}_N + (\Delta_{f_i} - \mathbf{I}_N)] \\ &= \sum_{i=1}^P h_i \mathbf{\Pi}^{l_i} + \sum_{i=1}^P h_i \mathbf{\Pi}^{l_i} (\Delta_{f_i} - \mathbf{I}_N) \triangleq \mathbf{H}'_t + \Delta \mathbf{H}_t. \end{aligned} \quad (56)$$

Assuming that  $|f_i|$  is a sufficiently small nonzero value,  $\Delta \mathbf{H}_t$  is close to  $\mathbf{0}_N$ . The matrix inversion in  $\mathbf{G}_t$  can be approximated using the matrix perturbation formula:

$$(\mathbf{H}_t \mathbf{H}_t^H + \sigma_n^2 \mathbf{I})^{-1} = (\mathbf{B} + \Delta \mathbf{B})^{-1} \approx (\mathbf{B}^{-1} - \mathbf{B}^{-1} \Delta \mathbf{B} \mathbf{B}^{-1}), \quad (57)$$

where

$$\begin{aligned} \mathbf{B} &= \mathbf{H}'_t \mathbf{H}'_t{}^H + \sigma_n^2 \mathbf{I}, \\ \Delta \mathbf{B} &= \mathbf{H}'_t \Delta \mathbf{H}_t^H + \Delta \mathbf{H}_t \mathbf{H}'_t{}^H + \Delta \mathbf{H}_t \Delta \mathbf{H}_t^H, \end{aligned} \quad (58)$$

and  $\Delta \mathbf{B}$  can be viewed as a matrix perturbation of the circulant channel matrix  $\mathbf{B}$ . It is worth noting that the above formulas take into account the scenarios where multiple paths with different Doppler shifts share the same delay tap.

Equation (30) implies that the magnitude matrix of  $\mathbf{T}_o$  with  $c_1 \neq 0$  is equivalent to the magnitude matrix of  $\mathbf{T}_o$  with  $c_1 = 0$  after undergoing a circular shift. Therefore, in order to simplify the analysis, we only analyze the case where  $c_1 = 0$ , and the analysis can be generalized to the case where  $c_1 \neq 0$  using circular shift operations.

Using the function  $\mathcal{I}_o(\cdot)$  in (27), we give the expression of  $\mathbf{T}_o$  with  $c_1 = 0$ , which is shown in (59). As  $\mathbf{B}^{-1}$  is a circulant matrix,  $\mathbf{F} \mathcal{I}_{o_1}(\mathbf{B}^{-1}) \mathbf{F}^H$  is a diagonal matrix. Given that  $|f_i|$  is sufficiently small, the magnitude of the elements in  $\mathbf{F} \mathcal{I}_{o_2}(\mathbf{H}_t) \mathbf{F}^H$  and  $\mathbf{F} \mathcal{I}_{o_3}(\mathbf{H}_t^H) \mathbf{F}^H$  fast decrease as the row-column relationship satisfies  $\min(|p-q|, N-|p-q|)$  increases. In other words, the two matrices can be approximated as quasi-band matrices with narrow bandwidth, as also observed in [13]. Therefore, as the product of the aforementioned three matrices,  $\mathbf{P}_1$  can be approximated as a quasi-band matrix, similar to the matrix product shown in Fig. 5. The analysis for  $\mathbf{P}_1$  can be extended to  $\mathbf{P}_2$ , which can be decomposed into the product of several diagonal matrices and quasi-band matrices with narrow bandwidth. Due to space limitations, we do not analyze  $\mathbf{P}_2$  in detail. Considering that the sum of quasi-band matrices is still a quasi-band matrix, we can assume that the high magnitude elements in  $\mathbf{T}_o$  with  $c_1 = 0$  for  $o \in \Delta_D$  are mainly concentrated within a finite region, where the row-column relationship should satisfy the condition that  $\min(|p-q|, N-|p-q|)$  is smaller than a certain threshold, as shown in *Observation 1*.

We consider a system with  $N = 256$ ,  $N/B = 1/15$  kHz,  $\text{SNR} = 10$  dB. This system is analyzed at two different maximum Doppler-shifts,  $f_{\max} = 3.7 \times 10^{-3}$  and  $7.4 \times 10^{-3}$ , corresponding to the movement speeds of 10 km/h, and 20 km/h, respectively. The magnitudes of the elements in  $\mathbf{T}_{o=1(128,:)}$  using the perturbation approximation given in (59) and the exact values are shown in Fig. 15. The figure demonstrates that the perturbation approximation is close to

the exact values, and also validates the effect of introducing small-scale Doppler shift to a static channel on the region containing high-magnitude elements.

According to (5), as the moving speed increases,  $f_i$  increases and the approximate analysis method may no longer be reliable. For high-speed moving scenarios, we provide statistical observations of 10,000 channel realizations. The mean magnitudes of  $\mathbf{T}_{o=1(128,:)}$  with different moving speeds are displayed in Fig. 16. The moving speeds are set to be 250 km/h, 350 km/h, 450 km/h, and 550 km/h, respectively. From the figure, we can observe that in scenarios with high moving speeds, the region of high-magnitude elements still follows *Observation 1*. This provides a basis for our chirp selection strategy in doubly selective channels.

## REFERENCES

- [1] Z. Li, X. Fang, H. Dong, C. Zhang, and X. Sha, "Chirp parameter selection for AFDM with MMSE equalization in static multipath channels," in *2023 IEEE Globecom Workshops (GC Wkshps)*, 2023, pp. 1099–1104.
- [2] Z. Zhang, Y. Xiao, Z. Ma, M. Xiao, Z. Ding, X. Lei, G. K. Karagiannidis, and P. Fan, "6G wireless networks: Vision, requirements, architecture, and key technologies," *IEEE Vehicular Technology Magazine*, vol. 14, no. 3, pp. 28–41, 2019.
- [3] K. Wang, X. Sha, L. Mei, and X. Qiu, "Performance analysis of hybrid carrier system with MMSE equalization over doubly-dispersive channels," *IEEE Communications Letters*, vol. 16, no. 7, pp. 1048–1051, 2012.
- [4] M. Martone, "A multicarrier system based on the fractional fourier transform for time-frequency-selective channels," *IEEE Transactions on Communications*, vol. 49, no. 6, pp. 1011–1020, 2001.
- [5] H. Ozaktas, O. Arikan, M. Kutay, and G. Bozdagt, "Digital computation of the fractional fourier transform," *IEEE Transactions on Signal Processing*, vol. 44, no. 9, pp. 2141–2150, 1996.
- [6] T. Erseghe, N. Laurenti, and V. Cellini, "A multicarrier architecture based upon the affine fourier transform," *IEEE Transactions on Communications*, vol. 53, no. 5, pp. 853–862, 2005.
- [7] S.-C. Pei and J.-J. Ding, "Closed-form discrete fractional and affine fourier transforms," *IEEE Transactions on Signal Processing*, vol. 48, no. 5, pp. 1338–1353, 2000.
- [8] D. Stojanović, I. Djurović, and B. R. Vojčić, "Interference analysis of multicarrier systems based on affine fourier transform," *IEEE Transactions on Wireless Communications*, vol. 8, no. 6, pp. 2877–2880, 2009.
- [9] D. Stojanović, I. Djurović, and B. R. Vojčić, "Multicarrier communications based on the affine fourier transform in doubly-dispersive channels," *EURASIP Journal on Wireless Communications and Networking*, vol. 868314, pp. 1–10, 2010.
- [10] X. Ouyang and J. Zhao, "Orthogonal Chirp Division Multiplexing," *IEEE Transactions on Communications*, vol. 64, no. 9, pp. 3946–3957, 2016.
- [11] M. S. Omar and X. Ma, "Spectrum design for Orthogonal Chirp Division Multiplexing transmissions," *IEEE Wireless Communications Letters*, vol. 9, no. 11, pp. 1990–1994, 2020.
- [12] R. Bomfin, M. Chaffi, and G. Fettweis, "Performance assessment of Orthogonal Chirp Division Multiplexing in MIMO space time coding," in *2019 IEEE 2nd 5G World Forum (5GWF)*. IEEE, 2019, pp. 220–225.
- [13] A. Bemani, N. Ksairi, and M. Kountouris, "Affine frequency division multiplexing for next generation wireless communications," *IEEE Transactions on Wireless Communications*, vol. 22, no. 11, pp. 8214–8229, 2023.

$$\begin{aligned} \mathbf{T}_o &= \mathbf{F} \mathcal{I}_o(\mathbf{H}_{eq}) \mathbf{F}^H \approx \mathbf{F} [\Pi^o \circ (\mathbf{H}_t^H \mathbf{B}^{-1} \mathbf{H}_t - \mathbf{H}_t^H \mathbf{B}^{-1} \Delta \mathbf{B} \mathbf{B}^{-1} \mathbf{H}_t)] \mathbf{F}^H \\ &= \sum_{[o_1+o_2+o_3]_N=o} \underbrace{\mathbf{F} \mathcal{I}_{o_1}(\mathbf{H}_t^H) \mathbf{F}^H \mathbf{F} \mathcal{I}_{o_2}(\mathbf{B}^{-1}) \mathbf{F}^H \mathbf{F} \mathcal{I}_{o_3}(\mathbf{H}_t) \mathbf{F}^H}_{\mathbf{P}_1} \\ &\quad - \sum_{[o_4+o_5+o_6+o_7+o_8]_N=o} \underbrace{\mathbf{F} \mathcal{I}_{o_4}(\mathbf{H}_t^H) \mathbf{F}^H \mathbf{F} \mathcal{I}_{o_5}(\mathbf{B}^{-1}) \mathbf{F}^H \mathbf{F} \mathcal{I}_{o_6}(\Delta \mathbf{B}) \mathbf{F}^H \mathbf{F} \mathcal{I}_{o_7}(\mathbf{B}^{-1}) \mathbf{F}^H \mathbf{F} \mathcal{I}_{o_8}(\mathbf{H}_t) \mathbf{F}^H}_{\mathbf{P}_2} \end{aligned} \quad (59)$$

- [14] Z. Sui, S. Yan, H. Zhang, S. Sun, Y. Zeng, L.-L. Yang, and L. Hanzo, "Performance analysis and approximate message passing detection of orthogonal time sequency multiplexing modulation," *IEEE Transactions on Wireless Communications*, vol. 23, no. 3, pp. 1913–1928, 2024.
- [15] T. Thaj and E. Viterbo, "Orthogonal time sequency multiplexing modulation," in *2021 IEEE Wireless Communications and Networking Conference (WCNC)*, 2021, pp. 1–7.
- [16] T. Thaj, E. Viterbo, and Y. Hong, "Orthogonal time sequency multiplexing modulation: Analysis and low-complexity receiver design," *IEEE Transactions on Wireless Communications*, vol. 20, no. 12, pp. 7842–7855, 2021.
- [17] G. D. Surabhi, R. M. Augustine, and A. Chockalingam, "Peak-to-average power ratio of OTFS modulation," *IEEE Communications Letters*, vol. 23, no. 6, pp. 999–1002, 2019.
- [18] W. Benzine, A. Bemani, N. Ksairi, and D. Slock, "Affine frequency division multiplexing for communications on sparse time-varying channels," in *GLOBECOM 2023 - 2023 IEEE Global Communications Conference*, 2023, pp. 4921–4926.
- [19] Z. Li, L. Ou, C. Zhang, X. Fang, and X. Sha, "A hybrid carrier communication system based on weighted affine fourier transform," *IEEE Communications Letters*, vol. 28, no. 7, pp. 1629–1633, 2024.
- [20] J. Zhu, Y. Tang, F. Liu, X. Zhang, H. Yin, and Y. Zhou, "AFDM-based bistatic integrated sensing and communication in static scatterer environments," *IEEE Wireless Communications Letters*, vol. 13, no. 8, pp. 2245–2249, 2024.
- [21] P. Raviteja, E. Viterbo, and Y. Hong, "OTFS performance on static multipath channels," *IEEE Wireless Communications Letters*, vol. 8, no. 3, pp. 745–748, 2019.
- [22] Y.-P. Lin and S.-M. Phoong, "BER minimized OFDM systems with channel independent precoders," *IEEE Transactions on Signal Processing*, vol. 51, no. 9, pp. 2369–2380, 2003.
- [23] T. Erseghe, P. Kraniuskas, and G. Carioraro, "Unified fractional fourier transform and sampling theorem," *IEEE Transactions on Signal Processing*, vol. 47, no. 12, pp. 3419–3423, 1999.
- [24] Y. Hong, T. Thaj, and E. Viterbo, *Delay-Doppler Communications: Principles and Applications*. Academic Press, 2022.
- [25] P. Raviteja, Y. Hong, E. Viterbo, and E. Biglieri, "Practical pulse-shaping waveforms for reduced-cyclic-prefix OTFS," *IEEE Transactions on Vehicular Technology*, vol. 68, no. 1, pp. 957–961, 2019.
- [26] A. Goldsmith, *Wireless communications*. Cambridge university press, 2005.
- [27] C. D. Meyer, *Matrix analysis and applied linear algebra*. Siam, 2000.
- [28] M. Benzi and N. Razouk, "Decay bounds and  $\mathcal{O}(n)$  algorithms for approximating functions of sparse matrices," *Electron. Trans. Numer. Anal.*, vol. 28, no. 8, pp. 16–39, 2007.
- [29] M. Matthe, D. Zhang, and G. Fettweis, "Iterative detection using MMSE-PIC demapping for MIMO-GFDM systems," in *European Wireless 2016; 22th European Wireless Conference*, 2016, pp. 1–7.
- [30] P. Schniter, "Low-complexity equalization of OFDM in doubly selective channels," *IEEE Transactions on Signal Processing*, vol. 52, no. 4, pp. 1002–1011, 2004.
- [31] I. Santos, J. J. Murillo-Fuentes, E. Arias-de Reyna, and P. M. Olmos, "Turbo EP-based equalization: A filter-type implementation," *IEEE Transactions on Communications*, vol. 66, no. 9, pp. 4259–4270, 2018.
- [32] S. Tiwari, S. S. Das, and V. Rangamgari, "Low complexity LMMSE receiver for OTFS," *IEEE Communications Letters*, vol. 23, no. 12, pp. 2205–2209, 2019.
- [33] A. Bemani, N. Ksairi, and M. Kountouris, "Low complexity equalization for AFDM in doubly dispersive channels," in *ICASSP 2022 - 2022 IEEE International Conference on Acoustics, Speech and Signal Processing (ICASSP)*, 2022, pp. 5273–5277.
- [34] S. Li, W. Yuan, Z. Wei, and J. Yuan, "Cross domain iterative detection for Orthogonal Time Frequency Space modulation," *IEEE Transactions on Wireless Communications*, vol. 21, no. 4, pp. 2227–2242, 2022.
- [35] Z. Tang, R. C. Cannizzaro, G. Leus, and P. Banelli, "Pilot-assisted time-varying channel estimation for OFDM systems," *IEEE Transactions on Signal Processing*, vol. 55, no. 5, pp. 2226–2238, 2007.
- [36] *LTE Evolved Universal Terrestrial Radio Access (E-UTRA); Base Station (BS) Radio Transmission and Reception*, Standard ETSI TS, 3GPP TS 36.104 version 14.3.0 Release 14, Apr. 2017.